Michigan Technological University

Michigan Technological University
Digital Commons @ Michigan Tech

Dissertations, Master's Theses and Master's Reports

2021

ANALYZING VARIATION IN DISPERSOID FORMATION IN ALUMINUM ALLOYS BY MINOR CHANGES IN HOMOGENIZATION TEMPERATURE

Brendan Treanore
Michigan Technological University, bltreano@mtu.edu

Copyright 2021 Brendan Treanore

Recommended Citation

Treanore, Brendan, "ANALYZING VARIATION IN DISPERSOID FORMATION IN ALUMINUM ALLOYS BY MINOR CHANGES IN HOMOGENIZATION TEMPERATURE", Open Access Master's Thesis, Michigan Technological University, 2021.
https://doi.org/10.37099/mtu.dc.etdr/1349

Follow this and additional works at: https://digitalcommons.mtu.edu/etdr

 Part of the Metallurgy Commons

ANALYZING VARIATION IN DISPERSOID FORMATION IN ALUMINUM ALLOYS BY MINOR CHANGES IN HOMOGENIZATION TEMPERATURE

By

Brendan Leith Treanore

A THESIS

Submitted in partial fulfillment of the requirements for the degree of

MASTER OF SCIENCE

In Materials Science and Engineering

MICHIGAN TECHNOLOGICAL UNIVERSITY

2021

© 2021 Brendan Leith Treanore

This thesis has been approved in partial fulfillment of the requirements for the Degree of MASTER OF SCIENCE in Materials Science and Engineering.

Department of Materials Science and Engineering

Thesis Advisor:	*Dr. Paul Sanders*
Committee Member:	*Dr. Dan Seguin*
Committee Member:	*Dr. Walter Milligan*
Committee Member:	*Thomas Wood*
Committee Member:	*Helen Weykamp*
Department Chair:	*Dr. Walter Milligan*

Table of Contents

Acknowledgements

Throughout this project and even my entire academic career I have received help from countless people who helped get me where I am today. It would be impossible to list all the people who helped me so I would like to thank everyone who has helped me throughout the years. There are some people who stand out amidst the past year that I would like to thank for their contributions to this project.

I would like to Norsk Hydro for the previous internships which led to the creation of this project. The funding and support I received from them made this project a reality and in turn let me make my contributions to the academic and scientific community.

I am thankful to Dr. Paul Sanders for supporting me from the first time I worked under his him my freshmen year to the endless guidance I received during my final year having him as my advisor to this master's degree.

Dr. Dan Seguin has been one of the most influential and helpful people in my department. I can say with confidence that many students, myself especially, would not be where we are today without him.

Various MSE staff played crucial roles in my work: Thomas Wood, Dr. Dale Dewald, Russel Stein, Liz Miller, Dr. Edward Laitila, the foundry co-ops.

The endless hours spent writing and working in laboratory would have been impossible without my friends and fellow students, Matt Hasbrouck and Emily Tom. I have worked harder alongside them than I would have ever been able to alone.

My family has supported me in ways no one else could and has been a constant pillar of support to me throughout the years.

Finally, I would like to personally thank Jessica Krycia, Nicholas Newberry, and Jared Edwards of the Michigan Tech Chemistry Department for helping me perform my phenol intermetallic particle extraction. They are the sole reason this valuable section of my research was completed and worked diligently to accommodate and assist me when no one else would.

Abstract

The homogenization of billets in the aluminum extrusion industry is a critical step that removes chemical segregation from casting, dissolves low melting point phases, forms nanoscale dispersoid phases, and promotes the ß → α transformation of iron particles in the matrix. With ever increasing use of aluminum extrusion in the automotive industry there is a constant need for increased efficiency and consistency in processing of extruded aluminum. The work in this thesis explores the effects of 10°C differences in the homogenization temperature on the formation of dispersoids in 6082 alloys used in the automotive industry. The role of dispersoids is to prevent the recrystallization of grains during extrusion giving a more uniform grain structure, improved mechanical properties, and improved corrosion resistance when compared to dispersoid-free alloys. This work found a 10°C increase in homogenization temperature resulted in a 5-15% decrease in dispersoid density, 5-10% increase in dispersoid size, and noticeable effect on mechanical and chemical properties. This effect was maintained regardless of the holding time, temperature, or ramp rate used for homogenization. Additional studies on the effects of two-step homogenizations found similar results on the variation in dispersoid density but had improved properties when compared to one-step homogenization cycles currently used in industry, shedding light on the importance of dispersoid nucleation mechanism in developing improved thermal processing of billets.

1 Introduction and Overview

1.1 Understanding Extruded Aluminum

Extruded aluminum is a ubiquitous engineering and architectural material that can take many different forms thanks to the unique process that is used to create it. Extrusion allows for the creation of long, continuous sections of metal with constant cross-sectional shapes. This process is used in the production of parts that could not be produced by nearly any other means and are heavily relied upon by numerous engineered products. In the United States, extruded products account for 28% of wrought aluminum consumption in 2015 according to a USITC report [1]. Aluminum extrusion has innumerable uses such as automotive body components, tubular commercial window framing, heat exchanges, hand rails, bicycle frames, piping or tubes, aerospace components, and consumer products to name a few [2], [3]. Production of extruded products is quite simple and has little variation between alloys and the shape of the extrusion. Extruded material begins as a cast billet of metal that is heat treated prior to extrusion process. Immediately before extrusion, the billet is preheated to a high temperature, around 450-500°C, which softens it considerably allowing for extrusion. The billet is placed in an extrusion press and forced into a die immense force, forcing the material through the die and shaping it into the final extrusion. Dies can be a variety of complex shapes including hollow tubes and very thin sections which is part of the versatility of the extrusion process [4]. A basic diagram shows this in Figure 1. While the process itself is quite simple, control over the

process parameters such as heat treatments, alloy chemistry, die design, extrusion temperature, and more create a near infinite number of variables that need to be considered for a quality extrusion.

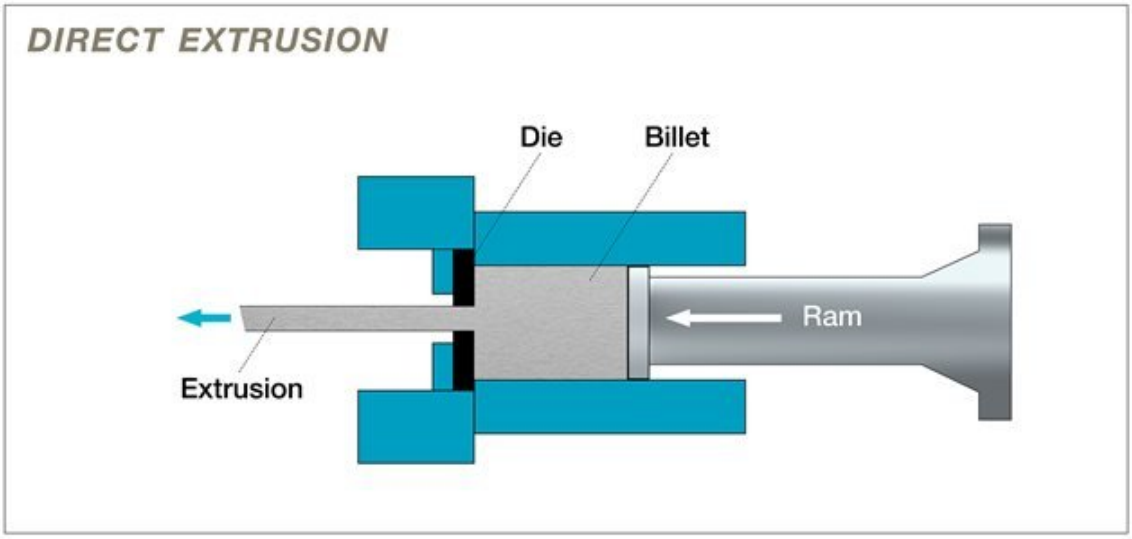

Figure 1. Basic diagram of the direct extrusion process [5]

1.2 Applications of Extruded Aluminum

As mentioned previously, extruded products account for 28% of wrought aluminum consumption in the United States. In industrial and commercial applications, where parts are often created on a large scale, the use of aluminum extrusions is prolific and plays a major role in the manufacturing of unique parts that would otherwise be costly or impossible to create. The ongoing work focused on light weighting vehicles has led to a major increase in the use of aluminum in the automotive industry. The ability to create complex hollow structures through aluminum extrusion has been used to lightweight body structures while simultaneously increasing the stiffness through design of these new structures [6]. While the automotive industry has only recently seriously considered the

applications of extruded aluminum, other industries have been using these same advantages for some time now. Many bicycle frames, from recumbents to mountain bikes, make use of extruded aluminum tubing that can take many shapes for optimized stiffness and lightweight design while keeping production costs low [7]. The flexibility in design of extruded aluminum makes it an incredibly attractive manufacturing process d that has proven its worth in many industries by making parts that no other methods can match.

1.2.1 Motivations for this work

With increasing use of aluminum extrusions in many industries there is a constant push for improving the quality, consistency, and reliability of this process. As with any large-scale production technique, consistency is the heart of creating a valuable end product. Improved process control is fundamental to this idea. There are many steps that influence the performance of extrusion, and these are detailed in the following section. In this study the focus is on the homogenization step which has many effects and is closely tied to extrusion performance and final quality of the extrusion. In alloys such as 6082 the formation of dispersoids occurs during homogenization which give the alloy the higher strength, corrosion resistance, and ductility that it is known for [8]. To better control the extrusion process, there is the need for better control over the heat treatment and formation of dispersoid particles. Temperature control is the more difficult half of the time-temperature dependence of any thermal processing in materials. This is exacerbated with increasing temperature where thermal variation can occur quickly and be difficult to

measure. Achieving tight temperature tolerance at the industrial scale of homogenization can be challenging and it has been observed that even small variations in temperature can have significant effect on dispersoid formation [9]–[11]. It is the purpose of this work to investigate and understand the effects of small temperature variations in homogenization furnaces to help refine industry practices. If the homogenization temperature of two 6082 type aluminum alloys is varied by 10-20°C then the observed dispersoid density will decrease by a significant amount because the higher temperatures will increase diffusion rate and dissolution of dispersoids.

1.3 The Life of a Billet

From casting to extrusion, the thermal history of an extruded part is vast but quite consistent between alloys. As shown in Figure 2**,** the thermal history of a part can be broken into 4-5 sections all which depend on the previous for producing high quality extrusions. Process variation, whether it be time, temperature, or speed, is unavoidable in every step but is considerably more important in some more than others. The effects of each step and the interactions it has with other steps is explained below.

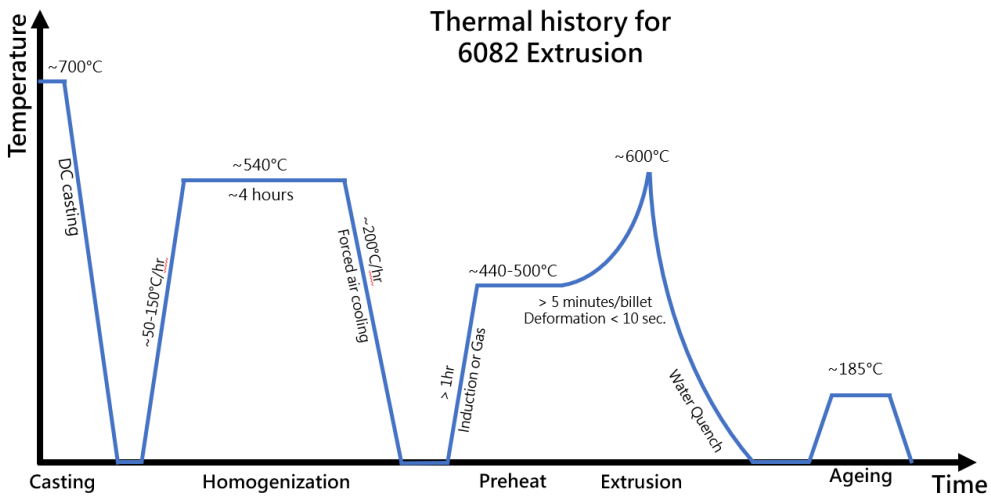

Figure 2. Thermal History of a 6082 Extrusion. Adapted from Reiso [12].

1.3.1 Casting

The complex geometries created by extrusion all start with the same indistinct cast cylindrical billets. Aluminum billets are typically cast using direct-chill casting, or DC casting, where the billets are vertically cast and drawn out through a water-cooled mold by a hydraulic ram which starts at the bottom of the mold. This casting method is extremely common in extruded aluminum and even beyond extrusion as majority of aluminum produced in the United States is produced by DC casting [13]. One undesirable effect of most casting processes, DC casting included, is segregation of alloying elements during solidification [14]. This segregation can lead to the formation of non-equilibrium phases and inconsistent chemistry, and thus chemical properties, across the radius of the billet [15], [16]. As solute atoms are rejected from the first to form dendrites of α-Al, the interdendritic region is enriched and upon solidification forms secondary intermetallic phases that are present throughout the microstructure.

1.3.2 Homogenizing

Homogenization is the step where billets are heat treated to form a microstructure that contains the desirable phases and is useable for extrusion. Homogenization begins with the slow ramping of the billets to the desired holding temperature, typically 500°C-600°C, where it is held for the desired homogenization time, typically 2-6 hours. Cooling is seen to have an effect of the precipitation of Mg_2Si and forced air is typically used to control the cooling of the billet over the course of multiple hours. Controlled heating and cooling rates are necessary for a homogeneous, uniform microstructure for good extrudability [4], [17]. The primary effects of homogenization is to reduce as-cast chemical segregation, dissolution of secondary phases, transformation of ß → α AlFeSi, and, in some alloys, form intermetallic nano-scale dispersoids [4], [18], [19]. The visible change in the microstructure from the as-cast state to homogenized can be seen in Figure 3.

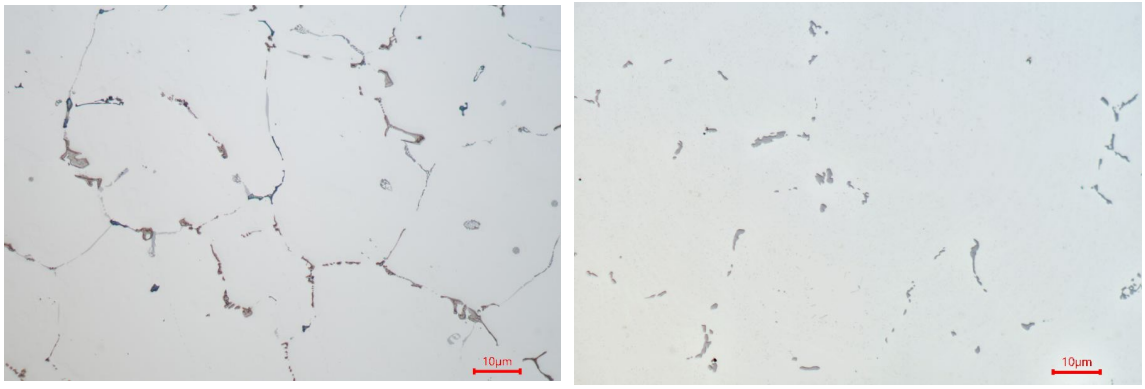

(a) (b)

Figure 3. 6082 billet microstructure in (a) as-cast state and (b) after a standard homogenization cycle showing the dissolution of many phases

Reduction of chemical segregation occurs during the homogenization process as elements go into solid solution and diffuse to create a more uniform distribution in solid solution. Complete dissolution of some phases occurs, leaving a fraction of the as-cast phases in the final microstructure, as shown in Figure 4. Presence of these soluble, low melting point phases, such as Mg_2Si, during the extrusion process is undesirable as high temperature deformation can cause local melting and tearing of the material, known as hot tearing [4]. During the formation of nano-scale dispersoids, presence of local chemical inhomogeneities can influence the formation of these particles creating an uniform distribution of dispersoids [20], [21]. The ß → α transformation of large, primary AlFeSi particles can improve overall extrusion performance and product quality by changing the morphology of sharp, stress concentrating ß-AlFeSi into rounded α-AlFeSi [22].

While the significance of each effect varies from alloy to alloy the overall importance of homogenization is the same. A tightly controlled homogenization process gives a high level of control over the microstructure and resulting properties of the billets during extrusion. It is for this reason there is an ongoing effort to better understand and optimize the homogenization process [16].

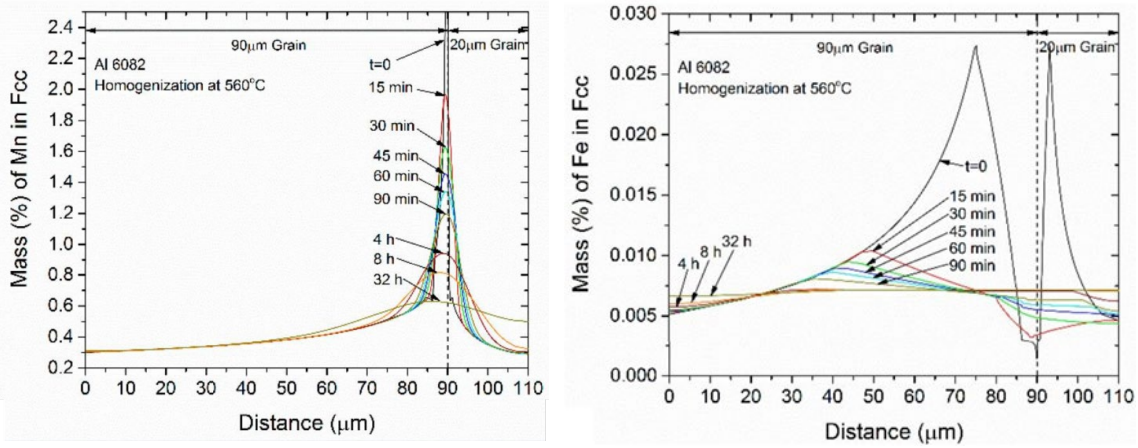

(a) (b)

Figure 4. Modeled effect of homogenization on Mn and concentration across grains in 6082. By Sarafoglou et al [23].

1.3.3 Preheat/Extrusion

Prior to extrusion, the billets are heated to the 'preheat temperature' which is usually the extrusion temperature, Figure 2 shows the thermal history of billets including preheat, in which dissolution of naturally precipitated Mg_2Si occurs. Incomplete dissolution of Mg_2Si can lead to hot tearing during extrusion so billet preheating times and temperatures need to be tightly controlled. Consistent billet preheating is crucial for maintaining a high quality, repeatable operation with maximum efficiency [24].

Small amounts of Mg_2Si will precipitate during cooling of homogenization but are controlled so preheating during extrusion redissolves them into the matrix. During extrusion, thermomechanical deformation during extrusion can lead to local increases in temperature up to 600°C causing melting of undissolved Mg_2Si phases [25]. During this time, intense deformation coupled with high temperatures can lead to dynamic

recrystallization. The presence of dispersoids in certain alloys can prevent recrystallization during extrusion resulting in a fibrous texture. Immediately after extrusion, the extrudate is typically water quenched to limit precipitation of strengthening phases for subsequent artificial aging [26].

1.3.4 Aging

The final step in thermal processing of extruded aluminum is typically artificial aging. After extrusion of 6000 alloys, it is desired that magnesium and silicon are fully dissolved in the microstructure as a solid solution. Artificial aging involves holding the material at ~185°C for ~6 hours to produce the optimum precipitation of the finely-dispersed Mg_2Si strengthening phase [26]. If water quenching after extrusion is not performed a solutionizing heat treatment to redissolve naturally precipitated Mg_2Si can be performed prior to aging. This artificial aging treatment is what gives the 6000 series aluminum alloys most of their strength.

1.4 6082 Alloy Microstructure

The processing of the 6000 alloy series has been explained in a general, but within the 6000 series there are many variations in the processing, design, and use of specific alloys. 6082 and 6110 alloys are higher alloy content 6000 alloys that are commonly used in the automotive sector due to their high strength and extrusion performance that can be controlled through the aforementioned dispersoid formation process during homogenization [27]. Control over the microstructure of these alloys is a complex

balance of maintaining extrusion performance and mechanical properties through optimized heating and cooling rates to meet customer specifications. No longer is the transformation and dissolution of phases the predominant process during homogenization, but in dispersoid containing alloys the formation of dispersoids has an equally important role in identifying the idealized heat treatment [21]. While higher temperatures can promote faster ß → α transformation and dissolution of phases it can also coarsen the dispersoid phases, reducing their effectiveness is stabilizing grain size and the impact of the alloy strengthening additions. It is necessary to find a balance between these competing processes to create the desired microstructure and properties for extrusion [15], [28].

1.4.1 Grain Structure

A defining characteristic of a dispersoid-containing extruded alloy is the unique fibrous structure that forms during the intense deformation. During extrusion there is sufficient deformation and heat that complete recrystallization and grain growth can occur leading to large, equiaxed grains. Additions of Mn and Cr creates dispersoids during homogenization which inhibit recrystallization and with sufficient dispersoid density can prevent it entirely, leading to a structure consisting of elongated grains with a 'fibrous' appearance. Experiments by Bru demonstrate the transition from a fibrous microstructure to a recrystallized one in Figure 5 [29]. The intense deformation and elongation of the original microstructure during the extrusion process are responsible for the elongated grains of the fibrous microstructure [15]. In Figure 6 that flow of material and the

resulting effect this has on the grain structure can be seen through a . This effect may be lost on the surface where the friction from the die surface and the shear forces acting on flowing metal can create much higher temperatures and strains. This increases the recrystallization driving force at the surface leading to a phenomenon known as 'peripheral coarse grains', PCG's, that recrystallize and grow exclusively at the surface of the extrusion [26]. The presence of PCG can cause issues during corrosion, bending, fatigue, and even issues surface finish [30], [31]. With a fully fibrous structure the toughness, ductility, and corrosion resistance of the extruded material increases significantly [15], [29], [32]. However, the presence of dispersoids in these alloys also increases quench sensitivity, work hardening, and flow stress during extrusion [27], [33], [34]. Thus, the ideal dispersoid density must balance optimized extrusion performance and grain structure. Once this criterion has been met, consistency in the homogenization process is needed to avoid variation in the dispersoid density which may influence extrudability and properties.

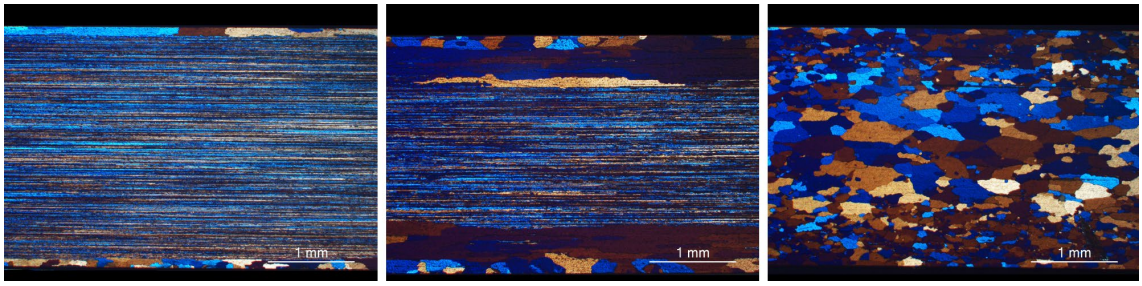

Figure 5. Extruded material etched to show various levels of recrystallization and fibrous structure, by Bru [29]

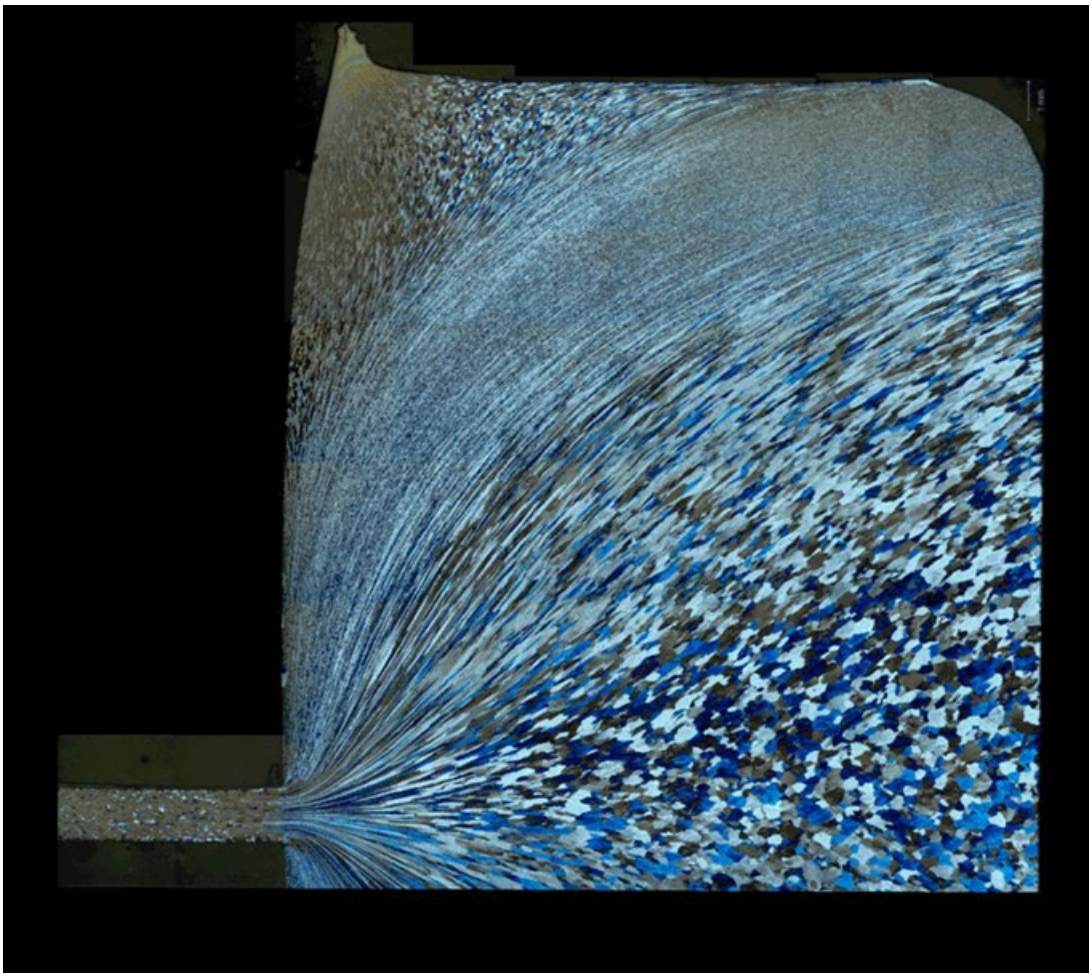

Figure 6. A half extruded billet showing material flow and grain structure changes that occur during extrusion. (Printed with permission from Dr. Trond Furu)

1.4.2 Mg_2Si

Like all of the 6000 series alloys, the strengthen of 6082 alloys comes from the precipitation hardening of Mg_2Si, which can occur naturally at room temperature or during artificial/elevated temperature aging. The prerequisite for precipitation is a supersaturated solid solution of Mg and Si, achieved by solutionizing to fully dissolve the Mg and Si and quickly quenching to trap these solute atoms within the matrix.

Solutionizing occurs in both homogenization and preheating prior to extrusion while quenching typically occurs immediately after exiting the die [35]. Diffusion kinetics of magnesium and silicon are sufficiently fast that even at room temperature there is appreciable natural precipitation and strengthening possible. This aging process is optimized at higher temperatures in artificial aging to increase strength and shorten the aging times to hours. Mg_2Si does not refer to a single phase but rather as series of phases the evolve during the aging process with continual nucleation and growth [36]. The full evolution of Mg_2Si is quite complex and involves 5 different metastable phases before forming equilibrium Mg_2Si [15]. It is beyond the scope of this work to focus on the exact precipitation kinetics and processes involved with the aging of 6082 material. In the as-cast state, however, the dissolution of Mg_2Si is important for extrusion performance and successful homogenization practices. Fortunately, in industrial practice where billets are larger and homogenization times are longer, the dissolution of Mg_2Si is often faster than the ß → α transformation given the high solubility and high diffusion rate of magnesium and silicon [15].

1.4.3 α/ß-AlFeSi Phase

The most abundant secondary phase in 6082 alloys by volume fraction is the AlFeSi iron phase. In this work this refers to the α & ß forms of AlFeSi which can take many morphologies depending on the processing and alloy content. Iron itself has extremely low solubility in aluminum and will form intermetallic phases with silicon, aluminum, manganese, and chromium upon solidification. Upon casting, the AlFeSi intermetallic

often takes the deleterious monoclinic ß form, Al_5FeSi, which has sharp corners that can cause cracking and reduce extrudability [17], [23]. Upon homogenization, as-cast ß transforms to the α form, which is most often reported as simple cubic or body centered cubic depending on chemistry and cooling rate [37], [38]. While the most commonly reported forms of AlFeSi are α and ß, based on stoichiometry other phases that have been reported across alloy systems and formation is highly dependent on processing and alloy composition.

1.4.4 Dispersoids and their Role

Dispersoids in the 6000's series alloy system refers to high-temperature, nanoscale, intermetallic precipitates that form during the homogenization process. Dispersoid formation in an alloy is usually dependent on the Mn and Cr content that leads to formation of Mn and Cr containing dispersoid phases during homogenization. On the scale of 5-200 nanometers in length, dispersoids form throughout the microstructure and can have a significant effect on the mechanical properties of an alloy. The main value in dispersoids is their high thermal stability which at temperatures where thermomechanical processing is performed. Homogeneously distributed dispersoids throughout the matrix can limit, or completely prevent, recrystallization during extrusion. The mechanism relies on creating a more homogeneous dislocation distribution that reduces nucleation points at dislocation pile-ups, and additionally, by prevents sub-grain growth through grain boundary pinning. The effect of dispersoids on hindering recrystallization is estimated using the Zener pinning pressure,

$$P_z = \frac{3F_v\gamma}{2r}, \qquad \text{Equation 1}$$

in which F_v is the dispersoid volume fraction, γ is the interfacial energy between the matrix and the dispersoids, r is the radius assuming a round particle, and P_z is the total Zener pressure opposing recrystallization [39]. This equation has been modified and used in many ways to consider shape, size distribution, and recrystallization driving force to better describe recrystallization behavior [38], [40], [41]. While no model has fully describes recrystallization behavior, it has been widely understood that increased dispersoid density can limit both recrystallization and growth during extrusion [21], [26], [29], [41]–[43].

1.4.5 Dispersoid Formation

The nucleation of these phases is first distinguished by the type of dispersoid forming, whether it be Cr or Mn containing, as these have proven to have unique nucleation routes. Work by multiple groups on the formation of Mn dispersoids has shown that *β'*-Mg_2Si phase acts as a nucleation site during homogenization. Considering the growth of Mg_2Si phase at lower temperatures, it was determined by Hu and Lodgaard that the heating rate during homogenization determines the growth, dissolution, and diffusion of Mg_2Si thus strongly influences the nucleation of Mn dispersoids on these particles. High heating rates during homogenization were shown to cause large dispersoid free zones (DFZ's) and form larger needle shaped dispersoids that were less effective at preventing recrystallization. Slower heating rates, coincidentally aligned with that seen in industrial large billet furnaces, favors a uniform distribution of fine Mn dispersoids in the

microstructure. Research on the formation of Cr dispersoids alone is limited compared to what is known on the formation of Mn-containing dispersoids. The diffusion kinetics of Cr is much slower than that of Mn and Cr dispersoid formation is often studied simultaneously with Mn dispersoids. Lodgaard found could not determine a clear formation route for Cr containing dispersoids, AlCrSi. There is increasing evidence of an intermediate phase, called the 'u-phase', which serves as a nucleation point for Cr dispersoids before dissolving during further homogenization [20], [41]. Understanding the nucleation of dispersoid phases is critical to controlling their size and number density with designed homogenization practices. However, in both Cr and Mn containing dispersoids, the nucleation and growth of these particles is difficult to study and remains a topic for further research for improving homogenization practices.

Measurement of dispersoid phases is most often accomplished using transmission electron microscopy (TEM) as they can as small as 5 nanometers in size. In many studies backscatter electron (BSE) mode on a Field Emission Scanning Electron Microscope (FESEM) is an alternative to TEM analysis for dispersoid characterization. This method is cheaper, faster, and easier to produce samples as compared to TEM. Recent work by Liu has found that for negligible difference between FESEM and TEM analysis [38]. Perhaps the largest issue with dispersoid measurements, regardless of the instrument used, are the frequently encountered issues with thresholding and image analysis; sample preparation, background noise, variations in brightness and contrast, minimum size threshold, variations in particle brightness, interaction volume, and particle shape all

complicate automated image analysis of dispersoids [37], [43], [44], [45]. From study to study it is unreasonable to expect similar measures of dispersoids given the number of variables, so fair comparisons are only possible within a single study or research group. One method that has only seen very limited use is etching for revealing and analysis dispersoid size and density. To the knowledge of the author, few papers have shown the use of etched dispersoid pits for analysis as it is mostly used to identify Dispersoid Free Zones (DFZ) with optical microscopy [8], [47]. Due to the somewhat unpredictable nature of etchants, especially at the nanoscale, it is preferrable to use BSE mode if sample preparation allows for it.

1.5 Alloying Elements

In the 6xxx alloy system the principal alloying elements are magnesium and silicon, which are employed for precipitation strengthening during artificial aging. Other additions such as iron, manganese, copper, and chromium have significant effects on the properties of the extruded materials through more complex relationships.

1.5.1 Iron

Iron is an intrinsic impurity in nearly every aluminum alloy due to the difficulty associated with removing it and its progressive accumulation during recycling of aluminum [48]. With very low solubility in aluminum even at high temperatures, iron typically forms intermetallic phases with Al and Si in the 6000's series alloys. The most common phases are the α/ß-AlFeSi that are formed during solidification [16]. Iron also is

found in dispersoid phases and plays an important role in deterimineing dispersoids and AlFeSi crystal structure [49]. It's been found that multiple AlFeSi phases can occur in the 6082 microstructure depending on the heat treatment and variations in the Fe content [37], [38]. Controlling the iron content of an alloy is important for controlling the secondary phases and dispersoids which have a significant role on the extrusion and final properties of the material.

1.5.2 Magnesium

Magnesium, along with silicon, are the primary alloying addition for precipitate strengthening in the 6000 series. Magnesium has significant solubility in aluminum and when in solution provides solid solution strengthening, like in the 5000 series which uses up to 5x as much magnesium as 6082**.** When silicon is in solid solution with magnesium the two will combine and grow to form various Mg_2Si phases through natural aging. The effect in solid solution, even for the 6000 series, needs to be considered for understanding the flow stress during extrusion. When magnesium and silicon are not in solution during extrusion and are instead precipitated as Mg_2Si, they can melt during the extrusion and lead to tearing.

1.5.3 Silicon

Silicon, unlike magnesium, has a role in multiple phases that are present in the 6082 alloy microstructure. Silicon levels in many alloys account for this by having excess beyond the 2:1 ratio that would be required for Mg_2Si formation. In the as-cast state

silicon is found in Mg_2Si, pure Si, and AlFeSi phases [37], [38]. During homogenization, dissolution of pure Si occurs as it goes into solid solution. According to Reiso, while in solid solution silicon provides strengthening that increases the required pressure for extrusion [4].

1.5.4 Manganese

Critical for dispersoid formation, manganese is intentionally added to alloys like 6082, 6005, and 6110. Other extruded alloys have some allowable levels of manganese but do not intentionally form dispersoids or derive any significant effect from them. Manganese is added for dispersoid formation but has other effects on alloy properties during extrusion. Increased Mn additions lowers extruded and aged material strength according to Bru and Furu [29], [50]. The most recent evidence by Furu finds that increased precipitate free zones, PFZ's, around dispersoids decreasing the available volume for Mg_2Si strengthening precipitates to form [50]. The benefits provide by dispersoid formation through manganese additions far outweighs the slight decrease in strength. Manganese also increases the quench sensitivity of extrusions, requiring fast cooling following extrusion to prevent Mg_2Si nucleation and growth on dispersoids [51].

1.5.5 Chromium

Similar to manganese, chromium is added for dispersoid formation during the homogenization treatment. Cr has been found to be less effective than Mn in forming dispersoids and is typically alloyed simultaneously with Mn. When alloyed with Mn, Cr

does not form Mn free dispersoids and instead only precipitates with Mn in the form of Al(FeMnCr)Si. Knowledge of the effect of Cr on dispersoid formation is still limited compared to Mn and research purposefully investigating the precipitation of Cr dispersoids has not always been successful [20], [52].

1.5.6 Copper

A minor alloying addition, in low amounts copper has been reported to drastically increase corrosion rate and provide some solid solution strengthening [15], [53]. The effect of copper on corrosion of 6000 alloys is severe in some cases as can lead to increased intergranular corrosion through the formation of a copper-rich film at grain boundaries. High amounts of thermomechanical processing, specifically extrusion, has been reported to limit the harmful IGC effect of Cu in 6082 alloys while simultaneously increasing strength [54].

2 Materials and Methods

Outlined below are the analysis methods used in this work. A general overview of the analysis performed is given here, while specific details on some methodologies are detailed in appendices. Restrictions on published information relevant to company sponsored materials and/or practices limit the specifics that can be given.

2.1 Billet Material and Cut Plan

Two 6082 type as-cast 8” diameter billets were supplied by Hydro’s casthouse in Henderson, KY. Alloy chemistry range is provided in Table 1. These two compositions, henceforth alloy 14 and alloy 16, had slices taken for heat treatment and the rest was kept for subsequent extrusion trials. The sampled slices were 35 mm thick for alloy 4 and 50 mm thick for alloy 6. For homogenization, the slices were cut into 20 pie-shaped sections of equal size; 15 were for one-step homogenization, three for 2-step, one kept as-cast, and one extra.

Figure 7. As-cast billets from Henderson (a) billet cut plan with 3 slices cut (b)

Thermocouple holes were drilled at the ½ radius approximately halfway into the samples for monitoring the homogenization temperature. Type K thermocouple wire was twisted to a junction and inserted into the drilled hole. To limit measurement error, aluminum foil was packed behind the wire to ensure contact between the thermocouple and the billet material. Readings without foil, depending on how they were secured in the hole, occasionally read the air temperature of the furnace, which was noticed when it changed faster than the billet slice temperature.

Table 1. Alloy Chemistry Range

Cast	Si	Fe	Cu	Mn	Mg	Cr
14	1.16	0.22	0.33	0.59	0.81	0.15
16	1.09	0.22	0.07	0.53	0.68	0.15

Following heat treatment, the samples were further sectioned for metallography, conductivity, hot compression, and XRD intermetallic phase analysis (Figure 5). For sample 14, a section was cut from the billet outer diameter using wire EDM to identify phases formed due to rapid surface cooling. Metallography samples were taken from the ½ radius area immediately next to the thermocouple reading. A 3 mm thick section was also cut from the entire surface of the wedge for conductivity measurements. Sample cut for metallography were mounted in epoxy and polished using the methods listed in section 2.3, Table 3.

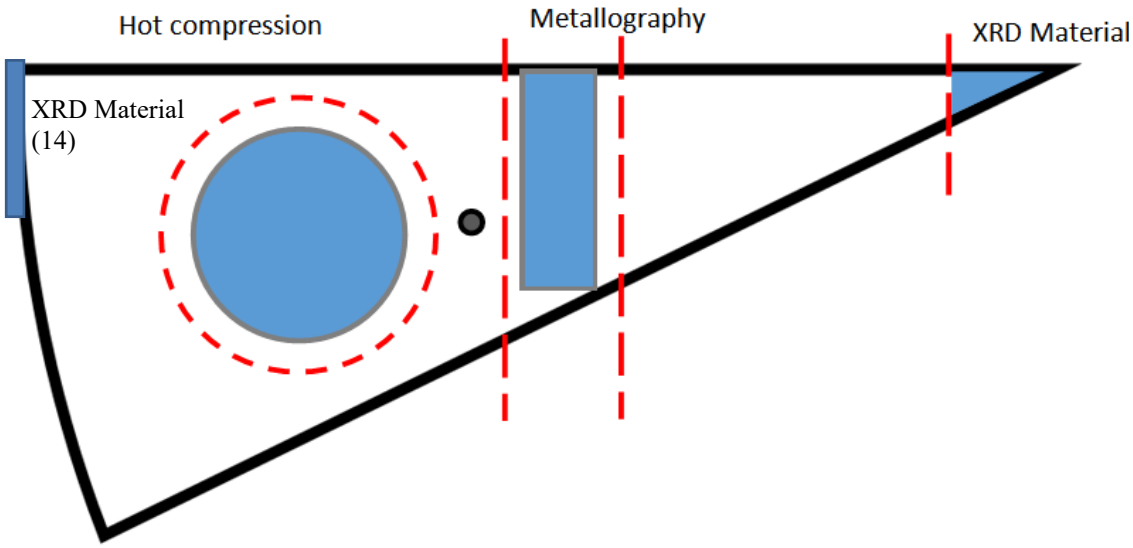

Figure 8. Sectioning plan for wedge sample. Section taken from the full surface plane for conductivity is not pictured.

2.2 Homogenization Plan

To assess the effect of minor oven temperature variations on the homogenization effectiveness, three different temperatures were tested at five different times, giving 15 one-step homogenization cycles (Table 2). Variations in production oven temperature (hot and cold spots) were used to determine the range of the homogenization temperatures, while times were based on common error states. The samples were put into a preheated furnace and soaking time was started when the measured temperature within 5°C of the setpoint. The heating time was not constant; 500°C was reached in 20-25 minutes and setpoint was reached typically within 50-60 minutes. Additionally, two-step homogenizations were tested to understand the benefit of distinct nucleation and growth temperature settings. The first soak temperature was 250°C for all samples, and the

second soak was at the same temperatures used for the one-step. (Table 3). After soaking for the listed time, the samples were removed from the furnace and quenched in water. The "zero" hour samples were quenched immediately after reaching the homogenization temperature.

Table 2. Homogenization Temperatures and Times

Temp / Time	550°C	560°C	570°C
0 hr	*Insufficient soak time, does not meeting industry standard*		
2 hr			
4 hr	**Target**	Excess Furnace Temperature due to 'Hotspots'	
8 hr	*Excess soak time*		
12 hr	*Billets held in furnace due to unexpected delays on mill floor*		
Two-Step Homogenization			
Controlled Ramp to 250°C, 2 hr hold, Ramp to…			
550°C, 3 hr		560°C, 3hr	570°C, 3 hr

2.3 Sample Preparation

Metallographic samples cut from the homogenized slices were taken from the ½ radius at the center of the thickness. They were mounted in cold-set epoxy resin in sets of three to limit the number of samples and maintain consistent surface area in polishing. Sample preparation for dispersoid analysis must be highly controlled as it can lead to differences in the measured dispersoid density. 9 samples were polished using a Leco AP-300 Autopolisher, with all materials and settings listed in Table 3. Between polishing steps, the samples were ultrasonically cleaned for 5-10 seconds in distilled water and then

immediately rinsed with ethanol. Samples were intended to be ultrasonically cleaned in ethanol but sufficiently large containers to fit the polishing head and ultrasonic bath could not be found and adding ethanol directly into the ultrasonic bath was a safety hazard. After 1μm polishing the samples were removed from the autopolisher and final polishing was done by hand as this step had the most significant effect on the quality of the polished surface and the apparent dispersoid density. The chemical-mechanical action of the oxide polishing solutions (OP-S) etches while polishing the surface leaving a nearly perfect finish but can lead to dispersoid pull out or etching at long times. After final polishing the pad was rinsed with DI water for 5 seconds at most to remove the OP-S, the sample surface was immediately wiped clean of OP-S using DI water and a clean glove and rinsed with ethanol. OP-S solution dries quickly and any that is remains the sample surface will cause serious issues with both the BSE and SE SEM analysis. For dispersoid analysis and phase identification, the samples were etched with a 0.5% HF solution for 7 seconds before being rinsed with DI water and ethanol.

Cylindrical samples for hot compression were cut on a mill with an annular cutter to according to the sample plan (Figure 5). The freestanding samples, still attached at the bottom, were sectioned off at 22 mm using an abrasive cutoff saw. The ends were then turned flat using a miniature metal lathe to approximately 21mm in length, giving right cylinders with a final diameter of 14 mm and a height of 21 mm and an aspect ratio of 1:1.5.

Table 3. Metallographic polishing materials and settings

Pad/Abrasive	***Lubricant***	***Time, Pressure***	***Speeds***
320 Grit SiC	Water	Until plane, 4 lb/sample	200 rpm, co-rotate
600 Grit SiC	Water	1 minute, 4 lb/sample	200 rpm, co-rotate
800 Grit SiC	Water	1 minute, 4 lb/sample	200 rpm, co-rotate
9 µm, TexMet-C	Allied RedLube	3 minutes, 5 lb/sample	200 rpm, co-rotate
3 µm, TexMet-C	Allied RedLube	4 minutes, 5 lb/sample	180 rpm, counter
1 µm, TexMet-C	Allied RedLube	5 minutes, 5 lb/sample	150 rpm, counter
0.05 µm Colloidal Silica	None	By hand, 45 seconds, light-moderate pressure	150 rpm, counter

2.4 Metallographic Analysis

Following polishing and etching, samples were analyzed for AlFeSi with light optical microscopy using a Nikon Eclipse MA100 and a Zeiss Axiomat at 500x for analysis of the secondary phase fraction and morphology. Images were taken from the unetched area for automated images analysis. Etched areas were used for phase ID in the as-cast and short homogenization time conditions. The software used for image analysis was Olympus Stream (Olympus Scientific Solutions Americas Inc.). Five images were taken per sample with similar conditions, autocorrected for contrast and flatness, and analyzed using an automated routine that measured 9 different metrics for the AlFeSi

morphology. The morphology metrics were particle count, total area, area fraction, elongation, shape factor, sphericity, perimeter, mean diameter, and max extent. Max extent was the maximum measure from one end of a particle to another. Mean diameter measured the diameter of a circle that was fit to the edges of a particle. Samples with additional intermetallic phases had their routines adjusted to avoid detecting these phases. Minimum object thresholds were set based on the observed particle sizes and the images were manually checked after automated analysis.

Scanning Electron Microscopy Energy Dispersive Spectroscopy, SEM EDS, was performed on the as-cast and homogenized samples for chemical analysis of phases that could not be identified with optical microscopy. An FEI Philips XL 40 Environmental Scanning Microscope was used at an accelerating voltage of 15kV to perform the EDS analysis. Dispersoid analysis was performed in the etched conditions using a Hitachi S-4700 at Michigan Technological University. Etching for 7 seconds with HF removes the dispersoids leaving holes that can be easily observed in SE mode. This time and concentrations were selected because they gave the closest match to the measures obtained in BSE mode. The BSE detector on this machine is not well suited for imaging nanoscale dispersoids at low accelerating voltages, and SE images could be acquired much faster with less setup and analyzed more consistently. To confirm the accuracy of the SE method, areas marked with microhardness indents were analyzed with BSE, etched, imaged in SE mode and then the images overlaid (Figure 6). This confirmed the size and location of dispersoids observed in BSE were those etched for measurement SE mode. After confirming the accuracy of the SE method, 10 images were taken per sample

with the settings in Table 4.Table 4. FE-SEM Operating Conditions for Dispersoid Imaging.

Hitachi S-4700 FE-SEM Operating Conditions	
Beam Mode	UHR-A
Accelerating Voltage	3.0 kV
Working Distance	10mm
Emission Current	10 nA
Condenser Lens 1 (Spot size)	7
Detector	*Lower* SE
Image Resolution	2560 x 1920, 8 bit Greyscale
Capture Time	80 seconds

Stage automation was not available on the Hitachi S-4700, so 10 locations were selected randomly, by hand, for every image on all 36 samples. To account for variable brightness and contract (BC) during imaging, an ImageJ plugin, *Stack Contrast Adjustment Plugin*, was used to normalize all images to a reference image [55]. Image analysis was done using Trainable Weka Image Analysis through ImageJ Fiji [56], and multiple images were used to train the classifier using an image set from which the reference image was taken,

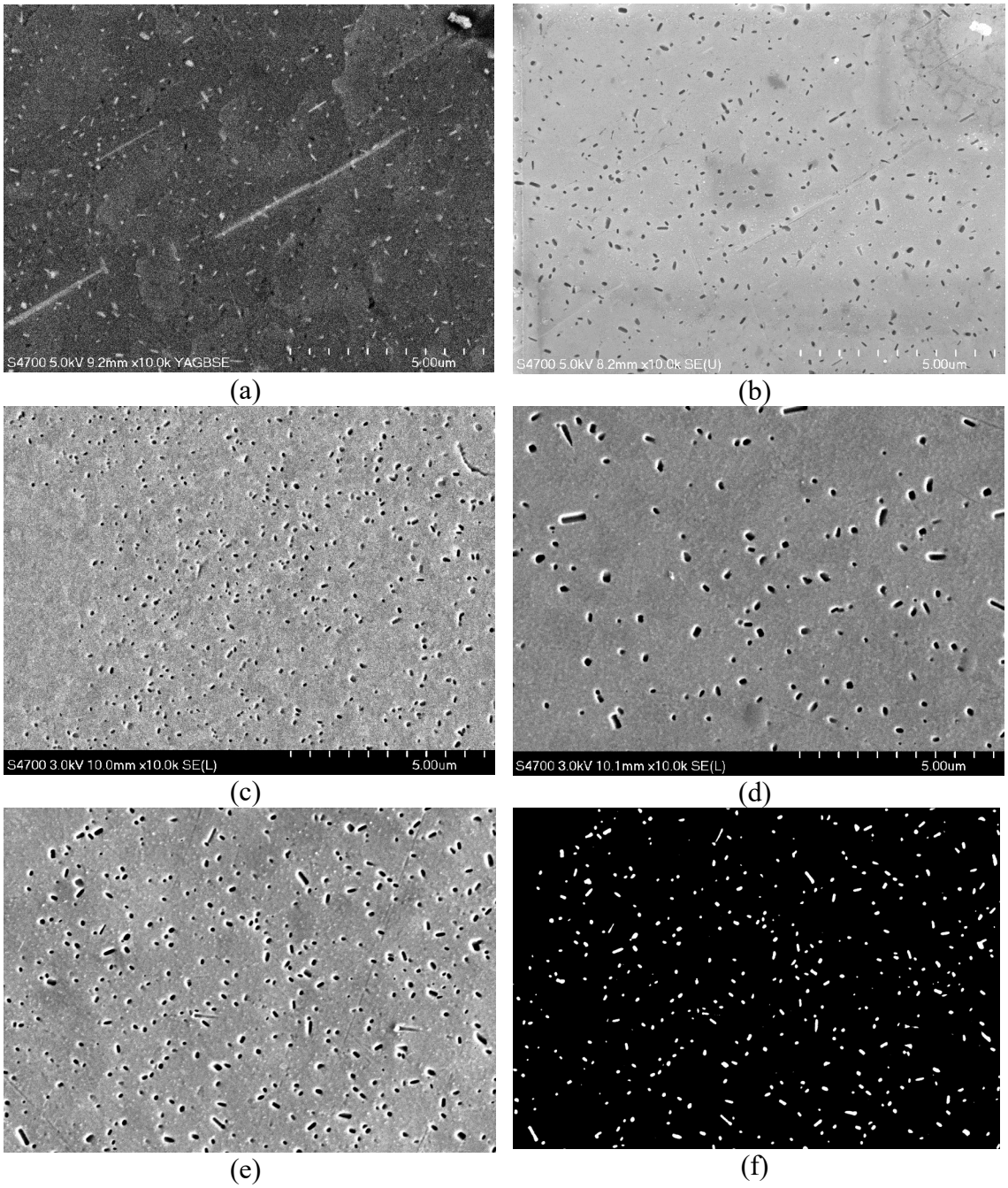

Figure 9. Unetched BSE image (a) Etched SE image of same area revealing dispersoids, note other phase unetched (b) Etched SE image of high dispersoid density (c). Etched SE image of low dispersoid density (d) SE Image before segmentation (e) Binarized image segmented by Weka

2.5 Hot Compression

The sample location for hot compression samples is detailed in Figure 5, with final slug height and diameter measured prior to compression in an Instron 4206 with a 10,000 pound load cell and long extensions so the platens could be held within a tube furnace. This setup is shown in Figure 11. The samples were held in the preheat furnace at 550°C for a minimum of 20 minutes and up to 40 minutes for the last samples to be tested. A thick aluminum plate with holes drilled to fit the slugs was used to limit heat loss during opening of the furnace. The tube furnace was preheated to 550°C, but after loading the sample and beginning the test the platen temperature was a consistent 530°C. The first samples tested were the 0 hour to limit the time it was held near homogenization temperature. After loading, the compression tests were performed at a strain rate of 10^{-2} s^{-1} until an engineering strain of 0.6 was achieved. Samples were immediately quenched after compression.

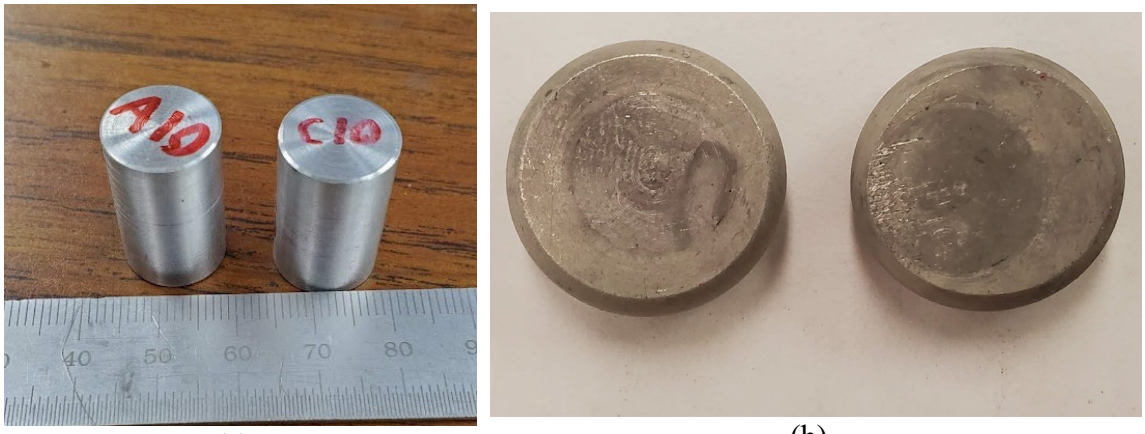

(a) (b)

Figure 10. Compression samples before (a) and after (b) testing

Figure 11. Hot Compression setup with tube furnace raised and removed for clarity

2.6 XRD Intermetallic Phase Extraction

To a facilitate a higher fidelity analysis of the intermetallic phases present in the as-cast billet, the molten phenol method for chemical extraction of intermetallics from the matrix was used. It was originally developed by Sato and Izumi [57], and progressively

refined by multiple researchers [47], [58]–[61]. Small chips of the as cast material were prepared by end milling at low RPM, creating chips approximately 1” long and 0.05 grams each. This method was found to be easier than the more standard microtome preparation. The chips were washed in ethanol and acetone using ultrasonic cleaning. Solid phenol (60 g) was melted in a round bottom flask with a condenser flowing cooled air attached to the top. A stirring bar was added, the phenol was heated to 170°C, and chips were slowly added to the round bottom flask to dissolve over 20 minutes. After full dissolution the heat was turned off, 100 ml of benzyl alcohol was added, and the mixture was placed in a Legend X1D centrifuge and spun at 8,000 rpm for 10 minutes. This process was completed with the assistance of colleagues in the Michigan Tech Chemistry Department who provided access to their centrifuge and materials. Excess solution was removed by pipetting and replaced with more benzyl alcohol. Centrifuging and adding more solution was then repeated twice with methanol. This method deviated from most as it allowed the solution to cool before centrifuging, but no issues were encountered due to the formation of aluminum phenolate that was encountered by other researchers. It was found that the presence of any water, as reported by Panahi recently and Satu and Izumi originally, is the most common issue with contamination of this experiment. The excess solution was extracted for the last time by pipette, and the intermetallic powder that settled at the bottom was allowed to dry naturally in open air. This powder was mixed thoroughly in a small container before packing onto a zero background powder holder for x-ray diffraction. XRD was performed on a Scintag Inc. (Division of Thermo ARL, Dearborn, MI) XDS-2000 Θ/Θ powder diffractometer. The beam used was Cu-K_α

radiation with nominal tube settings of 45kV and 35mA. Beam slits were 1-2 mm and receiving slits were 0.3-0.5mm with a graphite crystal monochromator. A scan was performed over a range of 10-70° with a step size of 0.01° and a count time of 10 seconds/step. The total scan time was 17 hours. The pattern was then analyzed using MDI Jade for background removal, peak identification, and phase matching.

(a) (b)

Figure 12. Glassware setup for intermetallic dissolution (a) and solution after addition of benzyl alcohol (b).

2.7 Conductivity

Conductivity was measured on a 4 mm thick slice taken from the homogenized sample surface. Conductivity was measured on all samples on the same day a minimum of 3 weeks after homogenization to allow for natural aging to stabilize the microstructure. Measurements were taken using a Sigmascope SMP10. Samples and the Sigmascope conductivity gage were allowed to come to thermal equilibrium with the room for 24 hours before testing was performed at 24.6°C. Three measurements were performed at the center of each sample.

3 Results

3.1 Phase Identification

Phases in the as-cast state were evaluated to understand the baseline material prior to changes that occur during homogenization. The results of XRD, optical microscopy, and SEM analysis are presented here. This data, combined with information found in literature, gives a full picture of the as-cast microstructural state of the alloys.

3.1.1 XRD

Initial evaluation of the as-cast material was performed with phase identification via x-ray diffraction of the extracted intermetallic phases. After the phases had been identified, whole pattern fitting (WPF) was performed to estimate the volume fraction of the phases of both alloys (Figure 9). From the scan, 51 significant peaks were identified in alloy 16 and of those, 47 of the largest were matched to phases. The good fit of phases matched to the peaks allowed for WPF to be performed giving an estimate of the volume fraction, crystallite size, and goodness of fit. The volume fraction of the intermetallics extracted from could not be provided for either sample because half of the solution was lost when some test tubes broke during initial centrifuging.

In alloy 16 the WPF revealed 76.9 wt% of the intermetallics to be α-AlFeSi, 13.4 wt% to be Mg_2Si, elemental Si to be 8.8 wt%, and the remaining fraction to be unidentified phases. The R/E ratio, a fitting metric in MDI Jade, was given as 1.4 indicating a high quality of fit, where a value of 1 indicates a perfect fit. The fit was

improved by splitting the α-AlFeSi into two distinct phases. A body centered cubic form and simple cubic form, both containing Mn, were found to provide the best fit. The exact phases used for fitting are provided in the Table 5 and Table 6.

For alloy 14, there were a total of 57 identified and of those, 7 were not identified but were found to be close fits with oxides. Mg_2Si and elemental Si were identified as they were in alloy 16. α-AlMnSi was found to be the primary intermetallic phase. In alloy 14 WPF revealed 91.9 wt% α-AlFeSi, 9.3 wt% Mg_2Si, and 2.3 wt% silicon. The R/E ratio was 1.33 indicating a good fit**.** In both alloys the presence of ß-AlFeSi was not detected in the XRD scans. Multiple phases of the form Al_5FeSi, $Al_9Fe_2Si_2$ were tested but significant peaks could not be found in either scan. The only phases identified with significant volume fraction were α-AlFeSi, Mg_2Si, and elemental Si.

The third sample tested was alloy 16, with a 2-step homogenization finishing at 550°C. This test was performed to understand if full dissolution of secondary phases such as Mg_2Si and elemental Si occurred during the homogenization treatment and to determine if any additional phase phases were forming. The pattern for this scan is shown in the appendix. The only phases that were identified in this scan were α-AlFeSi with the SC and BCC forms. No Mg_2Si, elemental Si, or any previously detected phases were present in the pattern.

Table 5. Alloy 14 Phases identified by XRD

Alloy 14 Intermetallic XRD Phase Identification				
Phase (Stoich.)	**Wt% (ESD)**	**PDF # Database**	**Bravais Lattice**	**Unit Cell Å**
α-AlMnSi $Al_{4.01}MnSi_{.74}$	79.8 (2.5)	01-087-0528	SC	12.604
α-Al(FeMn)Si $(Al_{19}Fe_4MnSi_2)_{5.31}$	12.1 (0.3)	01-071-4015	SC	12.619
Mg_2Si	5.6 (1.4)	04-002-0150	FCC	6.354
Si	2.5 (0.2)	04-001-7247	FCC	5.432

Table 6. Alloy 16 phases identified by XRD

Alloy 16 Intermetallic XRD Phase Identification				
Phase (Stoich.)	**Est. Wt%**	**PDF # Database**	**Bravais Lattice**	**Unit Cell Å**
α-Al(FeMn)Si $(Al_{19}Fe_4MnSi_2)_{5.31}$	21.3 (2.8)	01-087-0528	SC	12.58
α-Al(FeMn)Si $Mn_{.8}Fe_{3.2}Al_{17.1}Si_{1.9}$	55.6 (1.9)	04-009-3712	BCC	12.60
Mg_2Si	13.4 (0.3)	04-002-0150	FCC	6.35
Si	8.8 (0.2)	98-000-0396	FCC	5.43

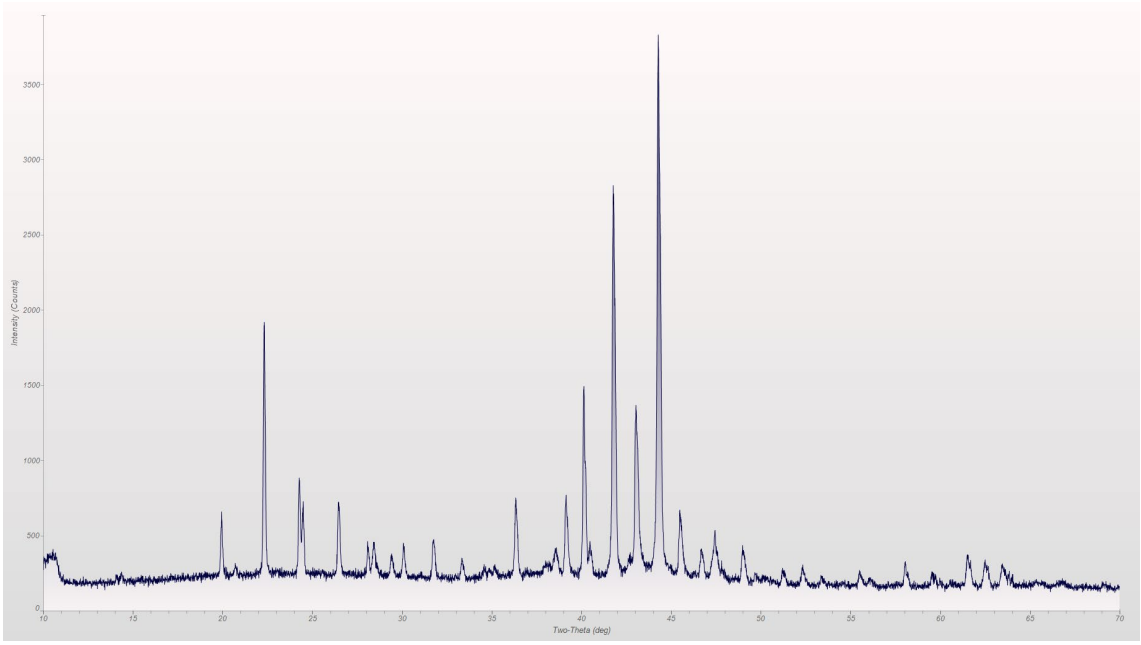
Intensity (Counts)
Two-Theta (deg)

(a)

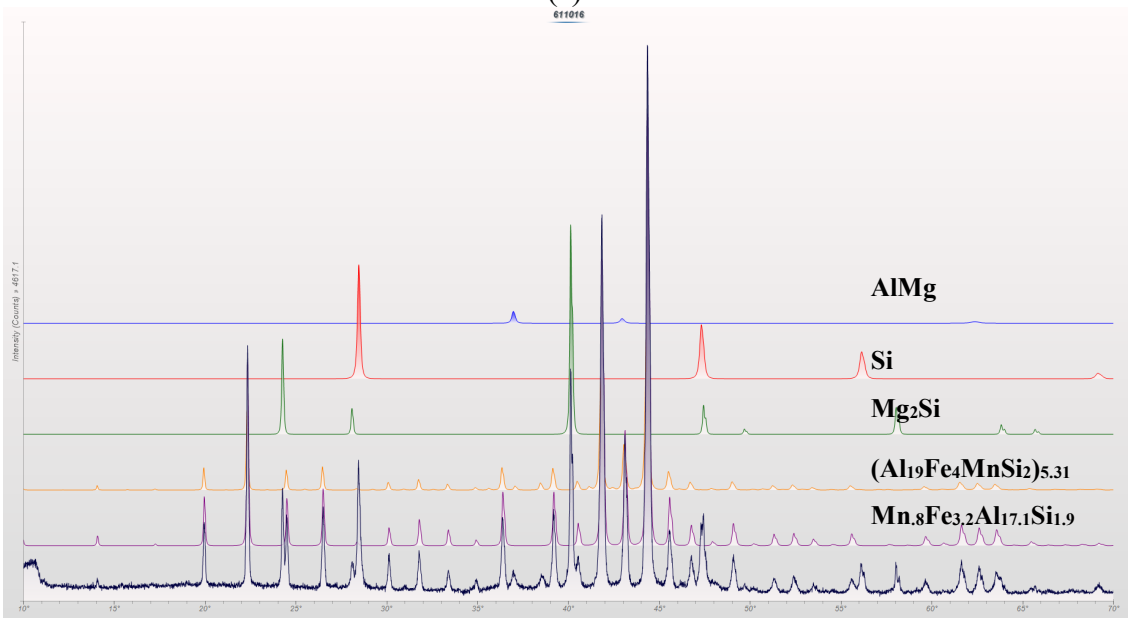
611016
Intensity (Counts) + 4617.1
AlMg
Si
Mg2Si
(Al19Fe4MnSi2)5.31
Mn.8Fe3.2Al17.1Si1.9

(b)

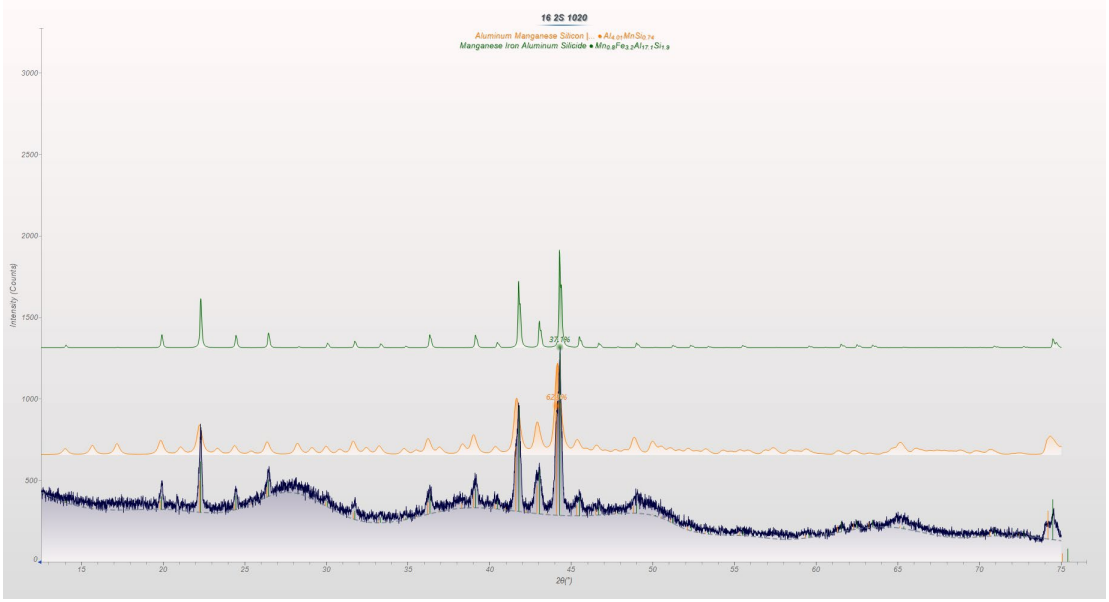

(c)

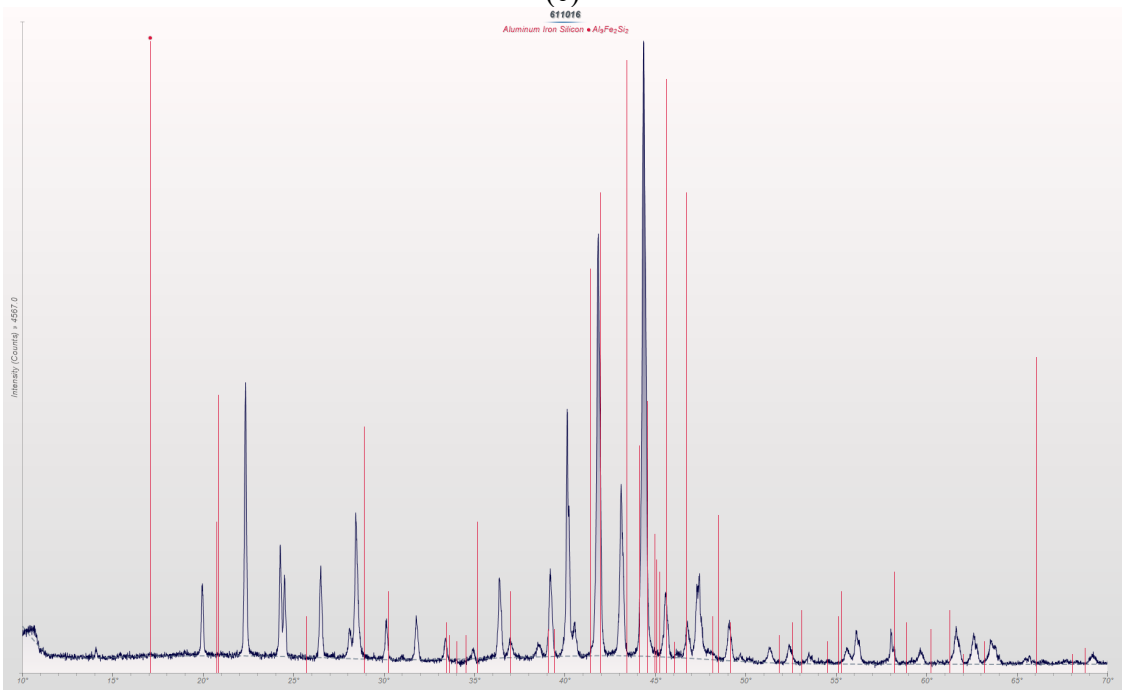

(d)

Figure 13. XRD pattern of extracted intermetallics for as-cast alloy 14 (a) and alloy 16 (b) 16 2-Step 550°C (c) and overlaid ß-Al_5FeSi peaks on the as-cast 16 pattern showing the lack of ß

3.2 Optical Microscopy and SEM EDS

Optical microscopy allowed for identification and morphological analysis of multiple phases in the as-cast material. Etching helped to distinguish phases that otherwise could not be seen. SEM EDS was used to check the chemistry and confirm phases which could not be identified by optical microscopy alone. In alloy 14, four categories of phases were identified: Mg_2Si, AlFeSi, Si, a less common grey phase which could not be identified through optical microscopy alone, and various regions that appeared to be ternary or quaternary reactions. The measurement of the AlFeSi morphology were complicated by additional phases present in the microstructure. The as-cast morphology of Mg_2Si and other phases was not measured, as they were seen to dissolve into the matrix during the 2-step homogenization x-ray analysis above. The morphology is presented in Figure 15and Figure 16 using various metrics used to describe the α-AlFeSi. This analysis could not be done on the as-cast samples due to the presence of other phases that could not be separated using thresholding. Various magnifications and areas containing multiple phases within the microstructure can be found in Figure 14. Annotations show the phases that were identified optical microscopy and SEM EDS [37].

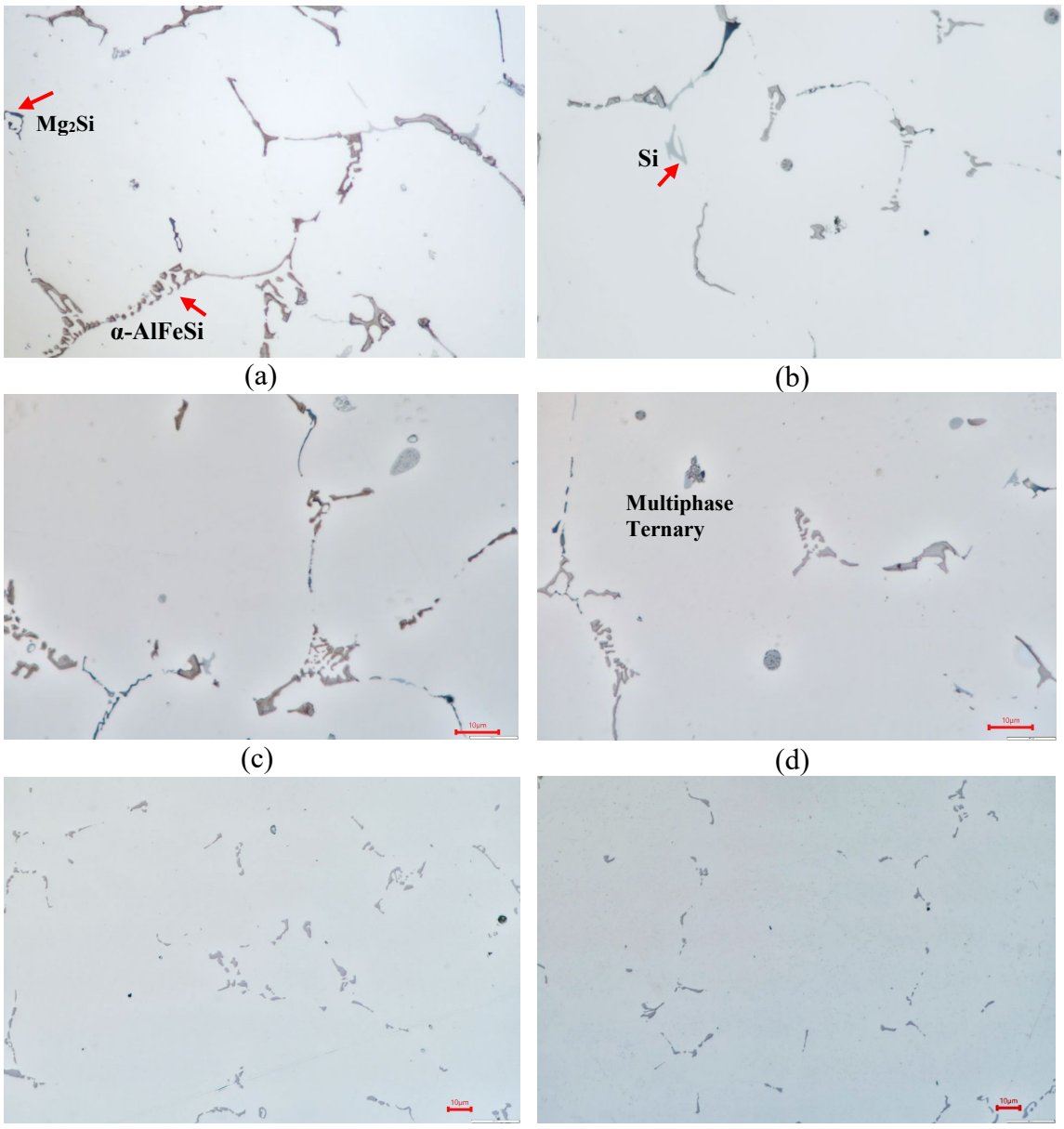

Figure 14. Optical microscopy after etching with 0.5% HF for 7 seconds: 14 as-cast with brown α-AlFeSi, black Mg_2Si, grey Si (a), 16 as-cast (b), 14 as-cast (c), 16 as-cast (d), unetched 14, 2-step 550°C (e) unetched 16, 8 hours 550°C (f) both homogenized showing only α-AlFeSi All scale bars are 10 µm.

Measurements taken on the AlFeSi phase in the homogenized condition are presented in Figure 15 and Figure 16. Comparisons are made between conditions of the same time and varying homogenization temperature. It is observed that little to no change occurs in these measurements regardless of the time or temperature of the homogenization condition. A small, but insignificant, increase in the mean shape factor is observed for both alloys correlated with increasing homogenization time. Decreasing perimeter and max extent was observed in both alloys but was also insignificant between temperatures.

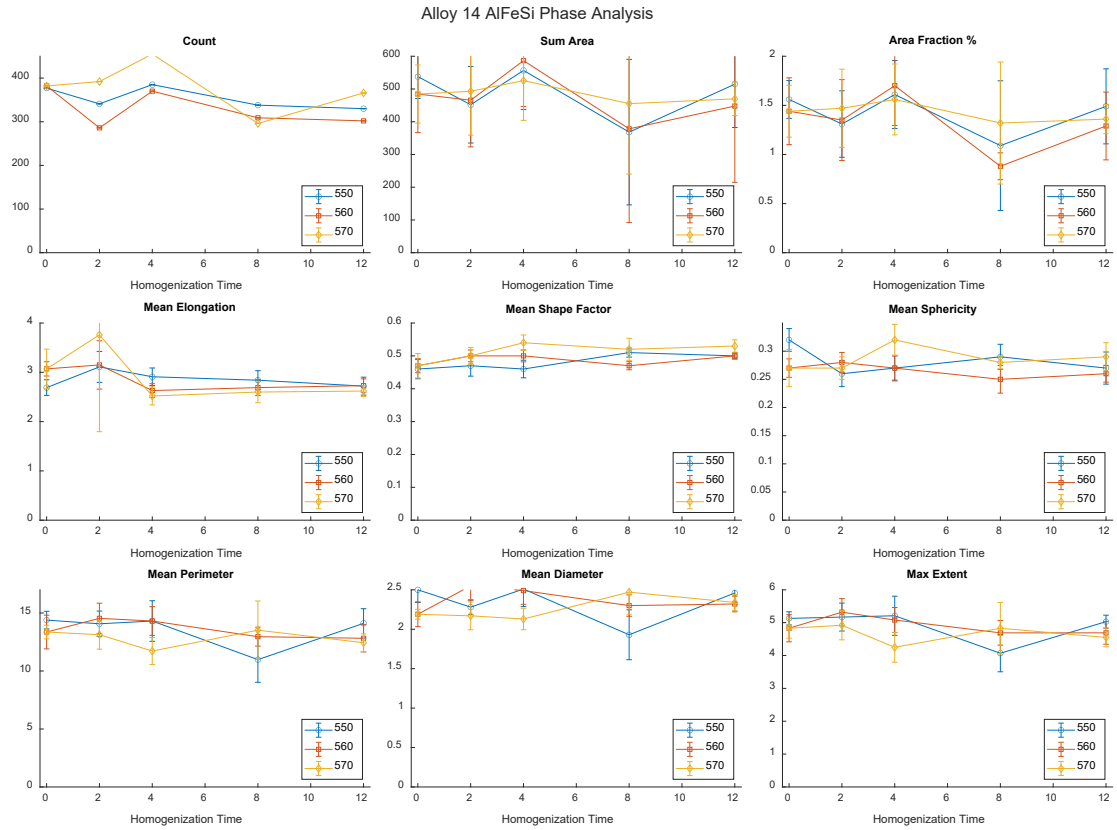

Figure 15. AlFeSi phase measurements for Alloy 14 in the homogenized condition.

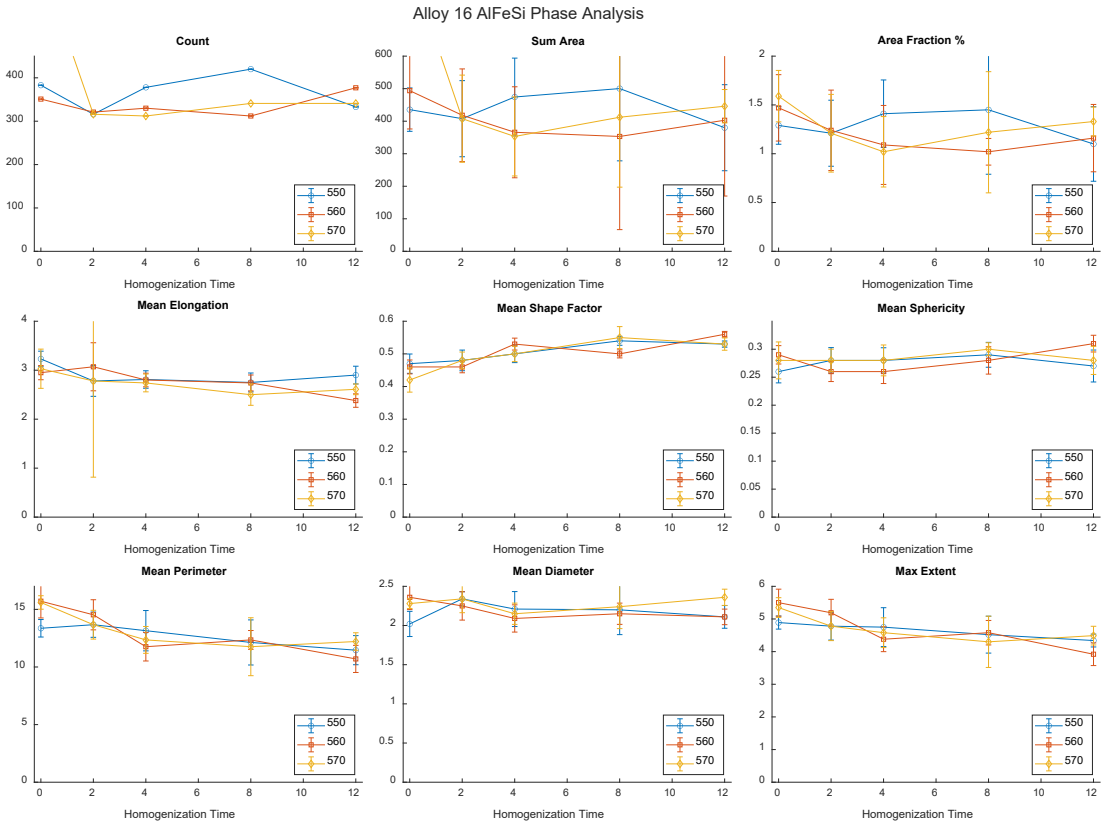

Figure 16. AlFeSi phase measurements for Alloy 16 in the homogenized condition.

SEM EDS of multiple areas was performed on the as-cast samples to identify the phases. Elemental maps were used to identify element distribution between phases while point scans gave approximate composition of the individual phases. In the as-cast state, the AlFeSi phase in alloy was found to contain Al(FeMnCr)Si but the composition could not be accurately determined. The interaction volume of the beam was larger than the phases being scanned giving high aluminum content for all phases. The approximate composition was found to be 15 wt% Fe, 10 wt% Mn, 5 wt% Si, and 70 wt% Aluminum. Some scans also indicated 1-2 wt% Cr. Alloy 14 was also found to have a AlCuMgSi phase with approximate composition of 10 wt% copper, 8 wt% magnesium, 10 wt%

silicon, and the remainder being aluminum. Finally, small round phases that contained most alloying additions were present in both alloy 14 and 16. From the EDS analysis it was determined both alloys contained Al(FeMnCr)Si, Mg_2Si, elemental silicon, and round multiphase phases. The as-cast state of Alloy 14 was found to have a CuMgSi phase that was not seen in alloy 16.

3.3 Dispersoid Measurements

Dispersoid measurements are presented as an equivalent circle diameter (ECD), which is the diameter of a circle with equivalent area as the particle measured. The minimum dispersoid size analyzed was limited to 30 nm ECD to avoid contributions from noise or polishing artifacts that were included in the image segmentation. A minimum size of 30 ECD was found to be near the minimum size observed in this alloy and this may be linked to the resolution limitations of the BSE or etching technique used to analyze it. Dispersoids are presented as histograms to show the distribution of dispersoid sizes and the number density as a function of time and temperature. Error is given as a 95% confidence interval for the mean dispersoid size in the histogram distribution and the dispersoid count in the number density. Two-step homogenizations are also presented with other conditions of the same temperature. The number density shown in Figure 17 is plotted with increasing homogenization temperature, rather than homogenization time, which is already well known to affect dispersoids. The 95% confidence interval for number density was calculated from the standard deviation of the dispersoid count from the 10 images.

To determine a mean dispersoid size, distribution width (s, sigma), and 95% confidence interval a logistic fit was applied in MATLAB using FitDist. While other researchers found a log-normal distribution to fit better, the limitations in measuring the smallest particles or the high heating rates used may have influenced the particle size distribution shape. This was found to give the best fit to the shape of the dispersoid distribution for most homogenization conditions. The two-step homogenizations are presented at the bottom as the slower controlled ramp rate, second soak, and overall time at temperature cannot be accurately compared to the one step conditions. The logistical function fit to the distributions provided a mean, sigma (scale parameter), and a 95% confidence interval for both. The sigma parameter describes the spread in the distribution and shape of the fit used. This shows the range of dispersoid sizes against the average.

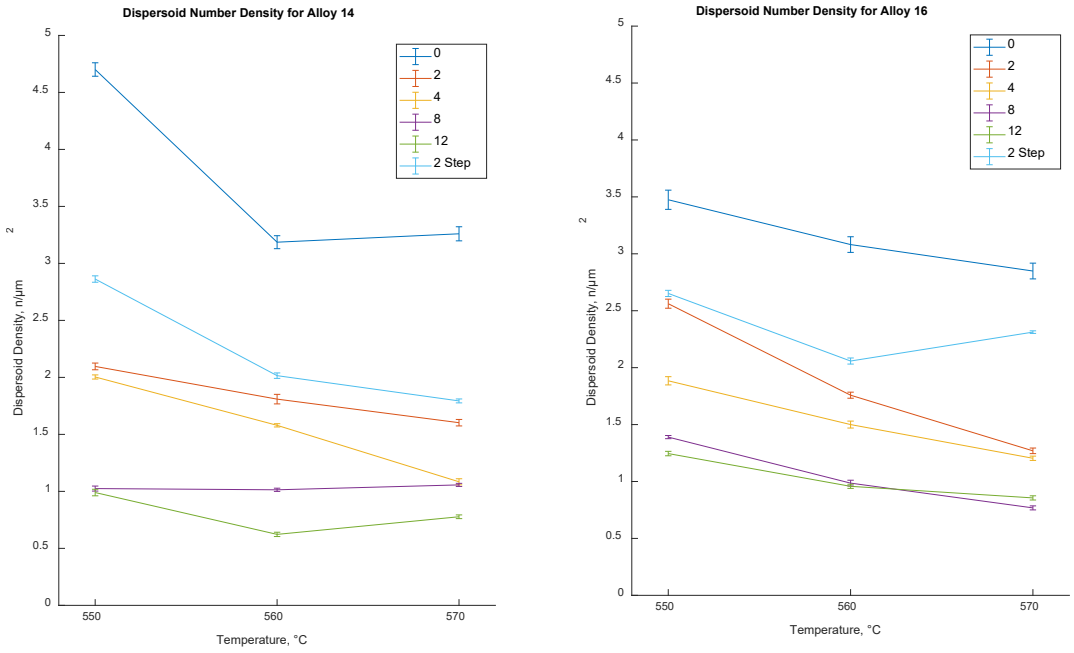

(a) (b)

Figure 17. Measured dispersoid number density for both alloys

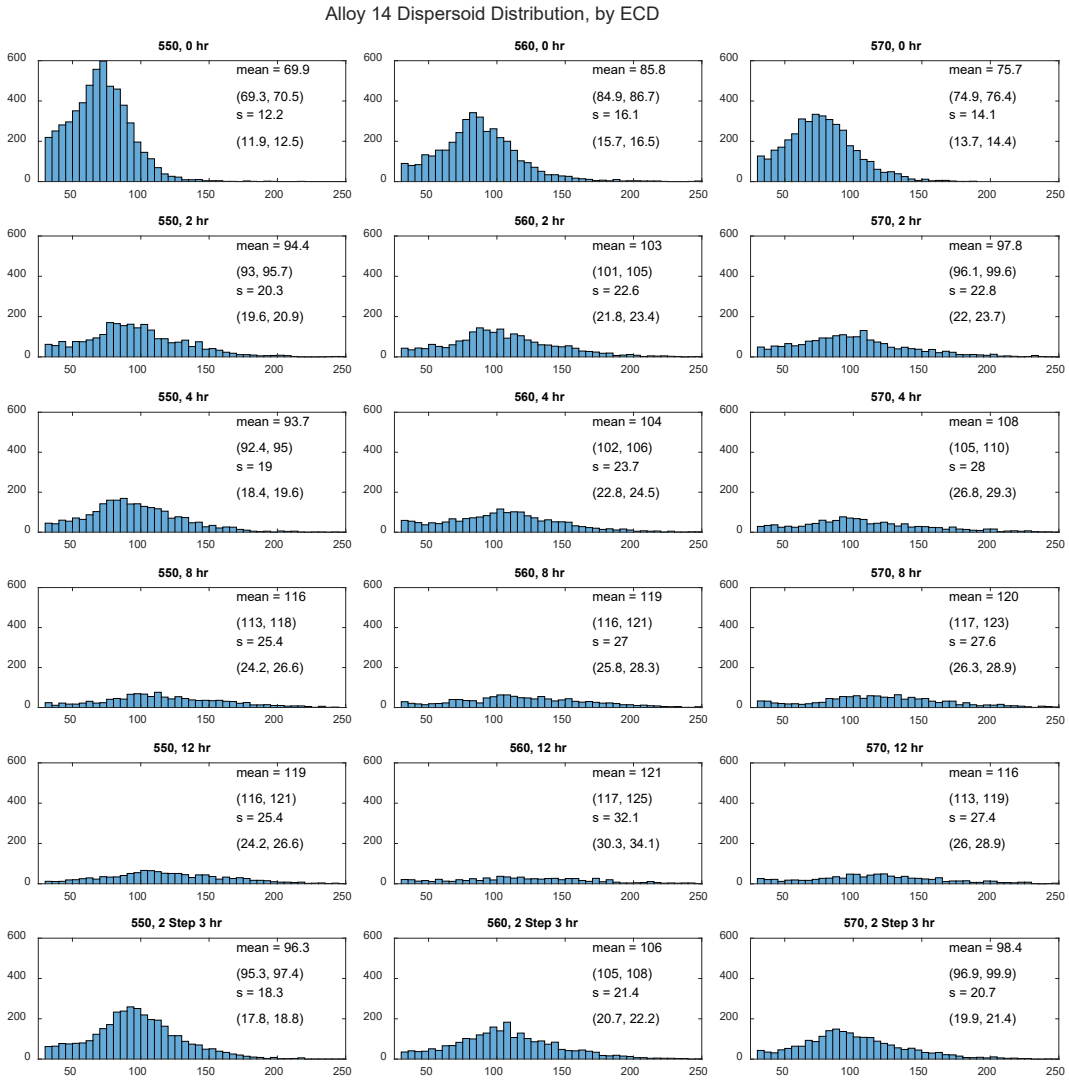

Figure 18. Dispersoid size distribution by count for alloy 14. Mean dispersoid size and standard deviation (s) 95% CI are annotated in each graph.

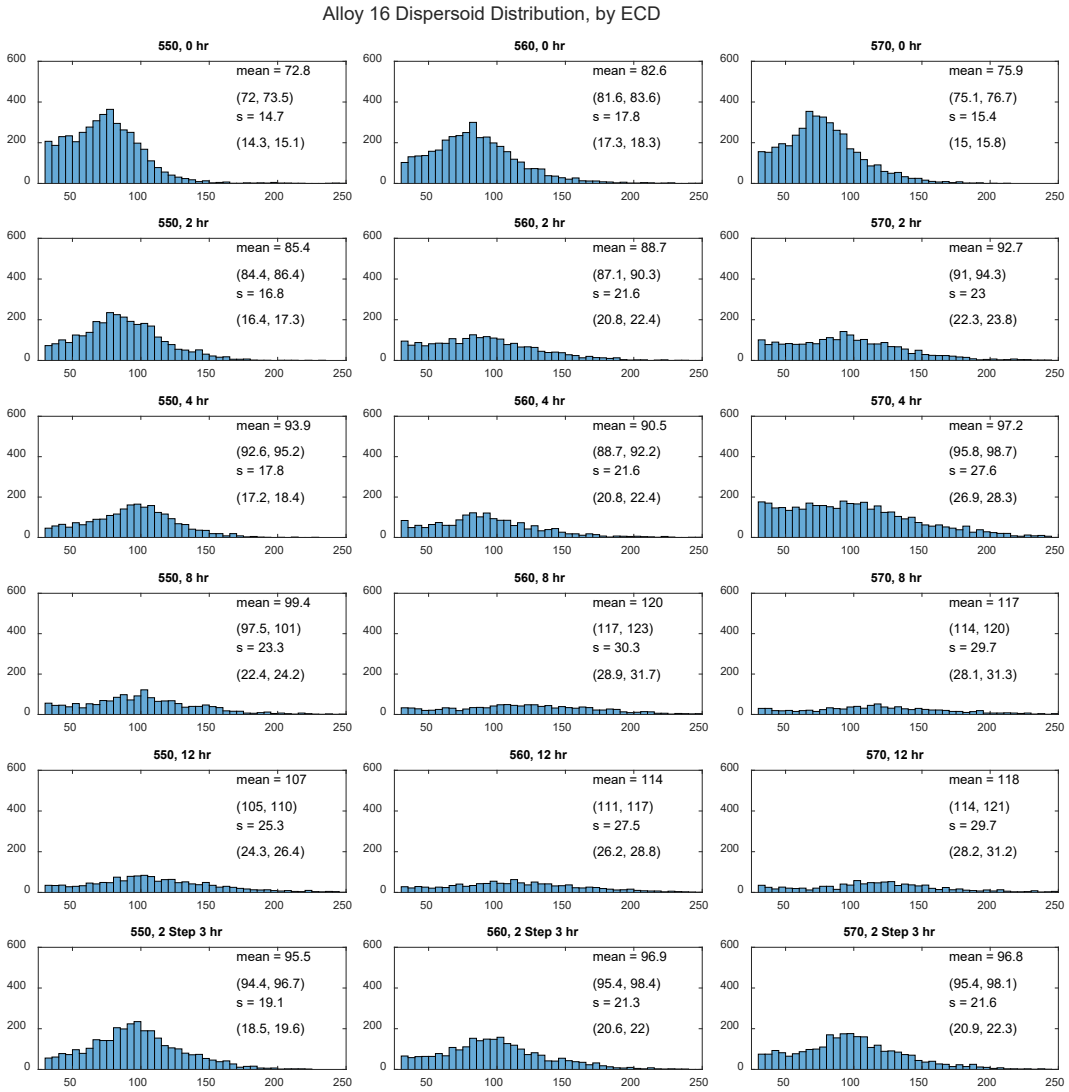

Figure 19. Dispersoid size distribution for alloy 16. Mean dispersoid size and standard deviation (s) 95% CI are annotated in each graph.

3.4 Hot Compression

Flow stress for the homogenized condition was measured with hot compression at 550°C. Testing consistency was complicated by temperature loss in the test apparatus while reloading samples. The compression platens were not perfectly parallel and

sometimes loosened between tests leading to nonuniform deformation, so steady state flow stress could not be achieved for all samples. Deformation was not uniform after the test and some samples showed asymmetric deformation as seen in Figure 16.

Figure 20. Concentric, uniformly deformed hot compression sample (left) and significant side slip and asymmetric material flow (right).

This non-uniform deformation of the samples made calculation of the true stress and strain inaccurate. Samples that exhibited uniform and concentric deformation showed a relatively flat steady state flow stress, but this was not the case for most samples. Due to issues with uniform deformation after yielding, only the yield strength and highest recorded flow stress were used to compare the hot compression strength of the samples. True stress and strain were used for this comparison. Samples were tested in sets of three with the intent to minimize the differences between samples at the same homogenization time. Samples in the 4 hour condition are shown in Figure 21 while other comparisons can be found in Appendix A, Hot Compression Results. The yield and approximated steady state flow, which was taken as the highest stress before the stress began to dip, are

tabulated in Table 7. An engineering strain of .6 was used to mark the end of test allowing for significant deformation in the samples. This was intended to induce recrystallization in the samples and give information on the recrystallization behavior based on dispersoid density. It was found that there was insufficient strain rates and total deformation for recrystallization to occur, even in samples with the lowest dispersoid density. Higher total strain and higher strain rates may allow for this to occur and serve as an additional method for analyzing recrystallization behavior, similar to extrusion.

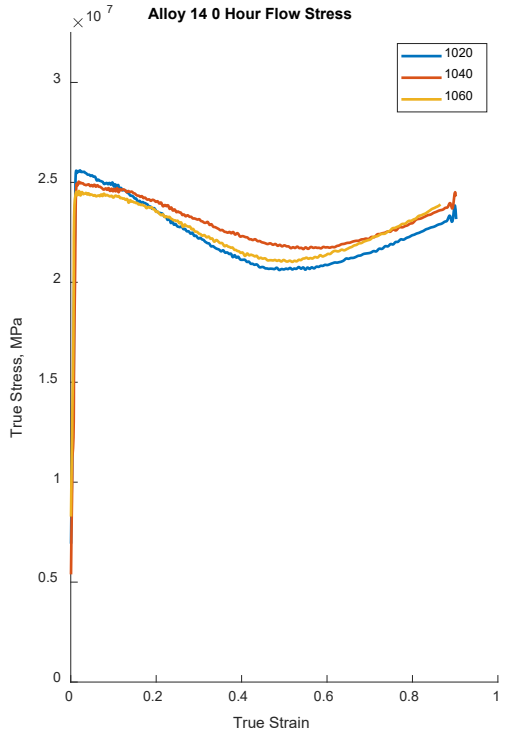

(a)

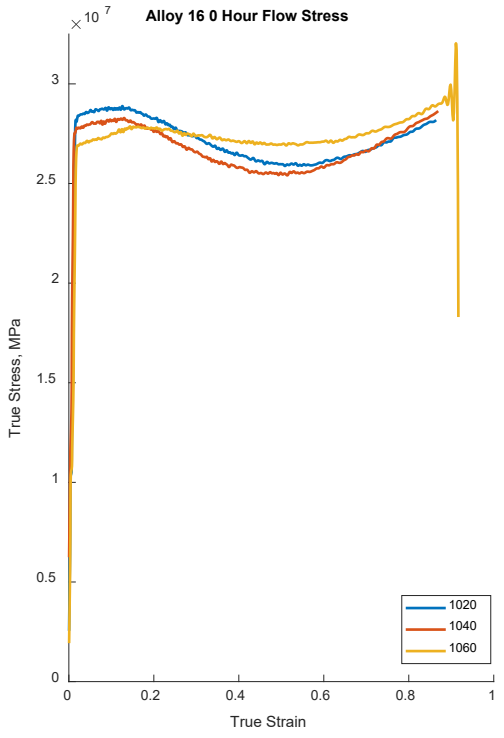

(b)

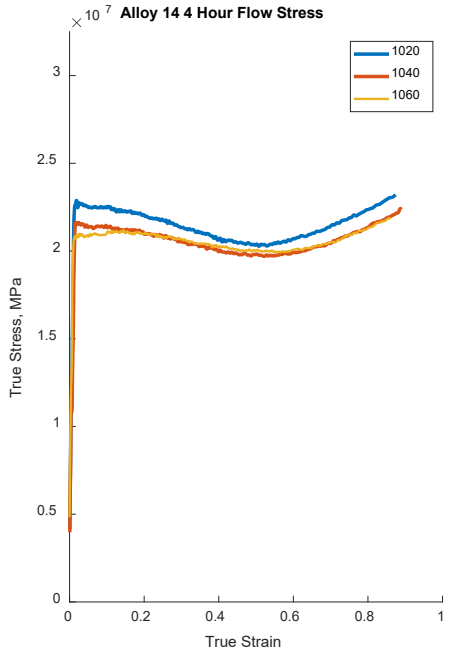

(c)

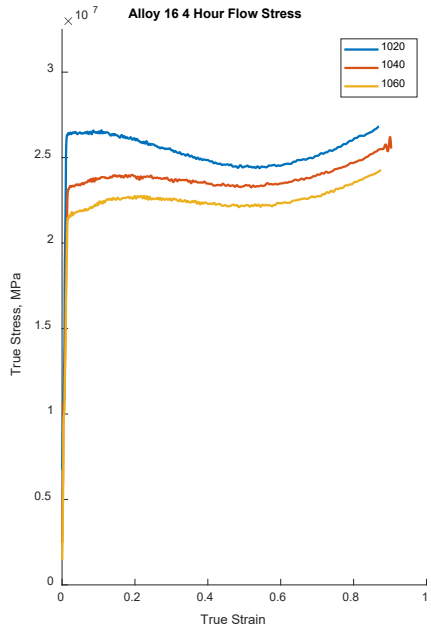

(d)

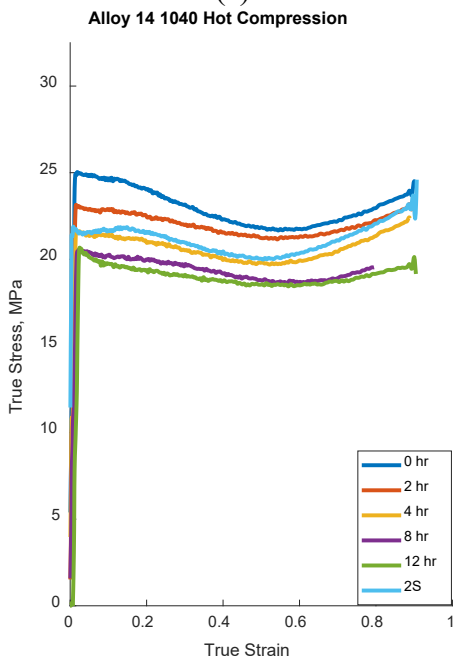

(e)

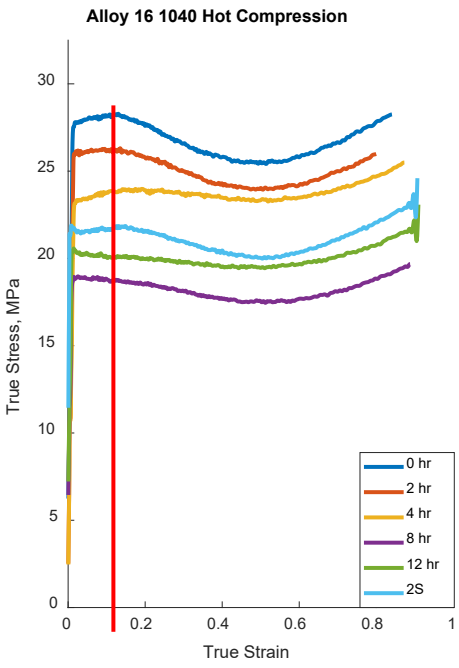

(f)

Figure 21. Hot compression true stress, true strain curves for alloys 14 and 16 plotted as a function temperature (a-d) and time (e-f)
The red line in (f) represents the point where flow stress was taken to avoid issues with non-uniform deformation that changed the calculated flow stress.

While the results of the hot compression are not entirely satisfactory, since true flow stress should have a flat steady-state region, conclusions can still be draw from the differences between the curves of the same homogenization times. The max true stress for the 5 different homogenization times, compared against the increasing homogenization temperature, shows Figure 22. The maximum true stress was taken as the highest value measured under .1 true strain, which is where deviation from regular deformation began to occur. A 95% CI could not be calculated as only one test could be performed with the available material. Alloy 16 was observed to have a higher flow stress than alloy 14, despite having a lower copper level which would lower solid solution strengthening. Alloy 16 testing was performed prior to alloy 14, and tests were performed at slightly lower temperatures, increasing the necessary stress for deformation. Alloy 14 had very consistent testing and a slightly higher temperature, which likely lowered the measured flow stress.

Table 7. Alloy 14 Max True Flow Stress under 0.1 (MPa)

550°C	560°C	570°C
26.3	22.7	20.8
25.6	23.3	21.5
25.4	22.0	17.5
24.0	21.9	20.8
23.8	21.6	22.8

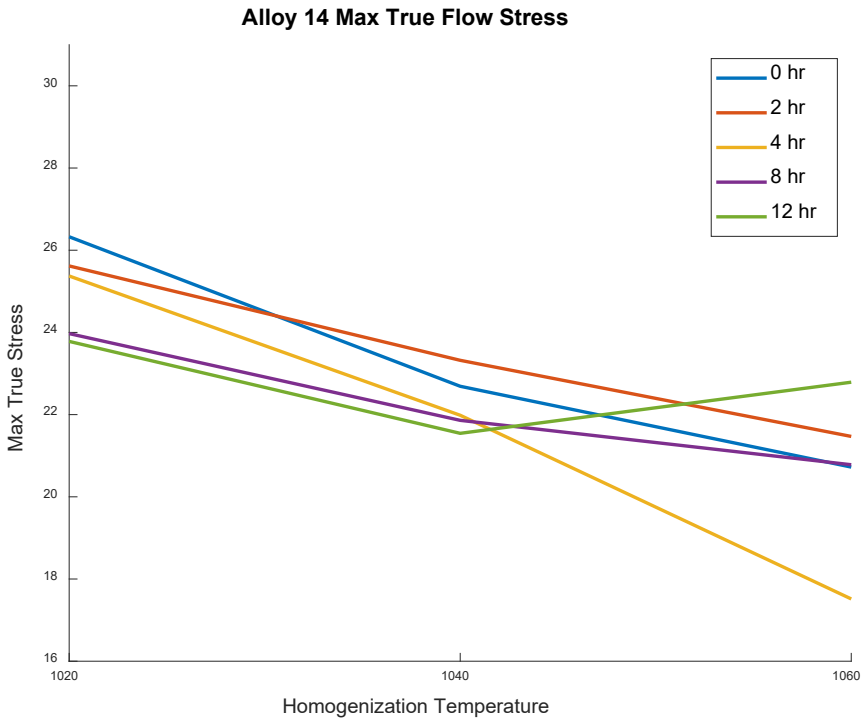

(a)

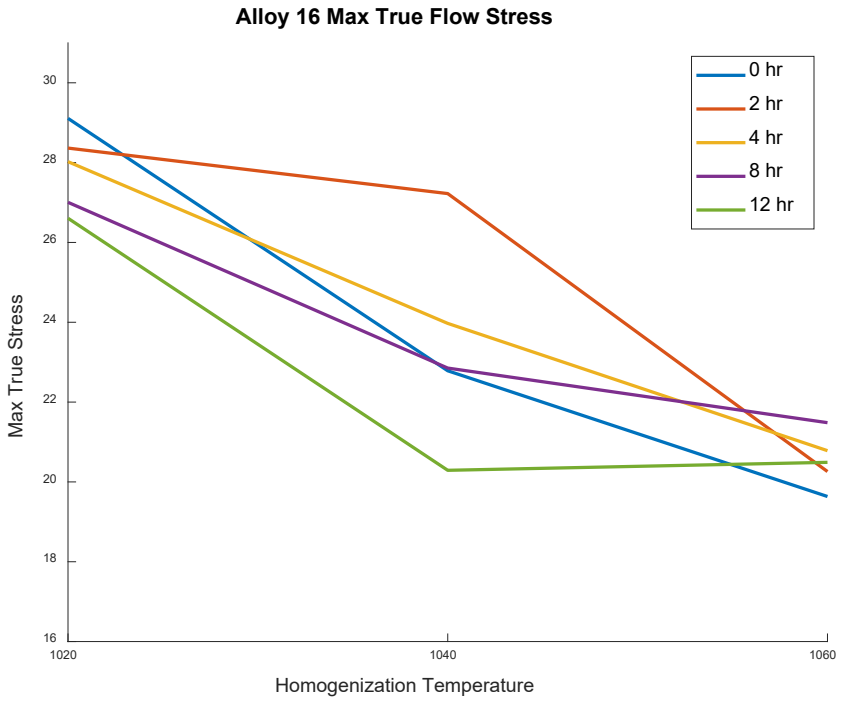

(b)

Figure 22. (a) Alloy 14 and (b) Alloy 16 Max True Flow Stress under 0.1 stress

3.5 Conductivity Measurements

Conductivity measurements were performed on all samples at the half radius as it was found that the measured value could change depending on location, likely due to differences in heating rates and quench rates at the surface and thinner areas of the slice. The three measurements taken are presented as a single average.

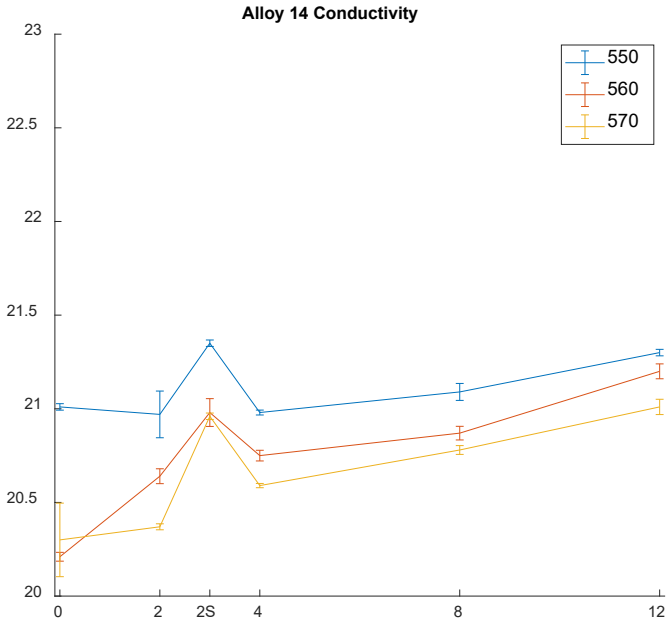

(a)

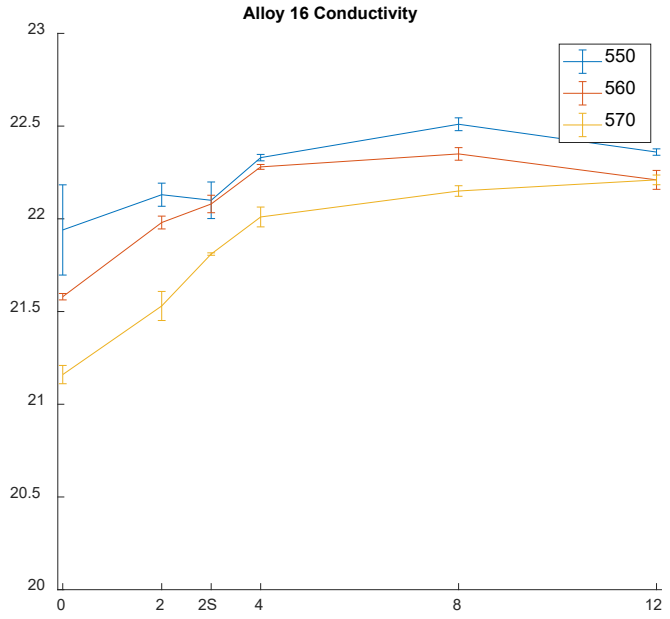

(b)

Figure 23. Conductivity (Ms/m) increase observed in observed with longer times and lower temperatures for (a) Alloy 14, (b) Alloy 16

4 Discussion

The primary objective of this analysis is to better understand the effect of homogenization parameters on dispersoid density, however, many other observed effects can be seen and correlated to this. Further, the addition of two-step homogenization practices allows for investigations into the effect of heating rate, holding time, and other phase transformations during standard homogenization treatments. Numerous studies over the years have analyzed dispersoid formation at various temperatures and times to explain the complex mechanics of dispersoid nucleation [20], [38], [45], [62]. Few, however, have looked specifically at the variation in dispersoid size at small differences in homogenization temperature as done in this study. Well below both the critical nucleation temperature of Mn (400°C – 460°C) and Cr (490°C – 580°C) containing dispersoids, the size and density is likely to be tied to growth and coarsening mechanisms[20]. However, given the high heating rates and wide range of holding times for the single step homogenization, nucleation will dominate for the shortest times while growth is more significant at the longest soak times.

4.1 Phase Transformation and Dissolution

4.1.1 XRD Analysis of as-cast Phases

XRD analysis of the extracted intermetallic powder from the as-cast material gave comprehensive understanding of the microstructure and phases present. In many 6000 series alloys, the transformation from ß → α AlFeSi is critical for producing quality high speed extrusion and determines the minimum homogenization time [15], [28]. The XRD

analysis found that in both as-cast alloys the ß-AlFeSi phase was not present at any detectable level. Multiple powder data files (PDF's) for the ß phase were tested, including Al_5FeSi and $Al_9Fe_2Si_2$, but no matching peaks were found in either sample. Use of the phenol intermetallic extraction method in other literature has documented its success in isolating the ß-AlFeSi phase if present [47], [57], [58]. It is possible that the formation ß-AlFeSi phase was suppressed during casting due to the high Mn content, high Mn:Fe ratio, and high cooling rates associated with DC casting of aluminum [63], [64]. Higher Mn contents primarily has been seen to promote the formation of α-AlFeSi during casting even with high Si content, which stabilizes ß [65]. Here, where the Mn content is significant for the formation of dispersoids, it appears the formation of ß-AlFeSi was suppressed to a level that was not detected in the XRD analysis. The sampling for alloy 16 was taken at the center of the billet, with the slowest cooling rate, while alloy 14 was taken at the surface where cooling would be nearly instantaneous. In alloy 16 the best fit was found using a simple cubic and body centered cubic α-AlFeSi phase while alloy 14 was best fit using only a SC α-AlMnSi phase. It has been reported that the α-AlMnSi phase is isostructural with α-AlFeSi and a wide range of chemistries is possible; thus the phases observed here are likely to be varying ratios of Fe:Mn depending on the cooling rate and local chemistry [66]. The BCC phase, however, was determined to be present given the additional reflections it presented in the diffraction pattern not observed in the SC phase. The other phases present in the as-cast structure, Mg_2Si and elemental Si, have significant volume fraction and are only observed in the as-cast structure. During homogenization, dissolution of Mg_2Si and Si occurs quickly, and

rapid cooling prevents precipitation of Mg_2Si. With the apparent lack of ß-AlFeSi phase in the cast structure, the minimum homogenization time for the alloys can instead be determined by Mg_2Si dissolution, rather than the ß → α transformation that governs homogenization times in other alloys. No other significant phases were found in either alloy, but some small peaks that best matched to various oxides, were present at very low volume fraction. This was seen more in alloy 14 where sampling was done at the surface of the cast billet. Alloy 14 also appeared to contain far less silicon and have the primary AlFeSi particles had a smaller unit cell after fitting was performed. This is believed to be caused by the higher cooling rates preferring the formation of a Mn rich AlFeSi phase rather than the balanced AlFeMnSi phase observed in alloy 16. In both as-cast samples some unknown peaks were present that could not be identified. The source of these was unclear but the assumed to be residual contamination from the extraction process. The size of the peaks was small and caused no significant issues with pattern fitting or phase fraction analysis.

The lack of Mg_2Si, elemental Si, and other phases in the post-homogenization scan indicate the heating rates and soak times are sufficient for full dissolution. The peaks identified for the α-AlFeSi were also found to be unchanged in their position suggesting the lack of any phase transformation occurring during the homogenization process. This analysis was not performed on the single step homogenization samples because the heating rates were dependent on the size of the sample and are unrepresentative of the heating rates that could be used in industrial applications. The slow heating of the two-

step homogenization, however, were similar to that which is used in industrial practices. An additional discovery made in the analysis of the homogenized two-step sample was the possible presence of dispersoid particles in the extracted powder. The peaks fit to the AlMnSi phase were much broader than the Al(FeMn)Si phase or those found in the as-cast samples. WPF showed the estimated crystallite size to be around 160nm compared to the > 1000nm estimated for all other phases. While crystallite size estimates can have considerable error, the magnitude smaller size and crystal structure suggesting greater Mn contents would imply the observed particles here are dispersoids. Observations of the powder in using an FE-SEM seemed to confirm this. Various submicron particles were found throughout the powder dispersoid on carbon tape and matched the shape which was seen in dispersoid analysis. Previous use of the phenol extraction method considered it impossible to analyze submicron particles however the methods and results here show that it is possible and estimates of the size can be achieved with XRD or FE-SEM observation [58]. It is possible that the size of the particles makes them subject to Brownian motion so they cannot be separated from solution unless bound to a larger particle or the solution is boiled, where they may be found on the edge of the container in a fine layer. A picture of the extracted dispersoid particles is shown below.

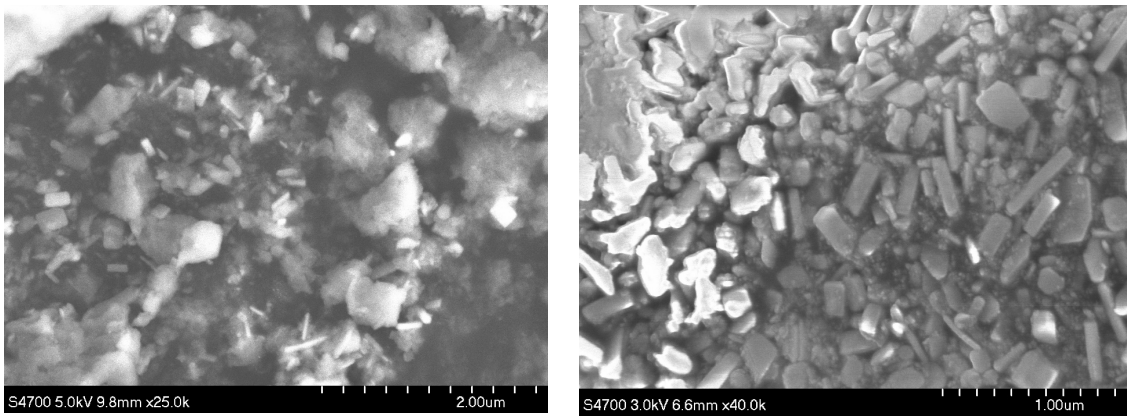

Figure 24. FE-SEM images of possible dispersoids extracted from a homogenized sample on carbon tape. Particles stuck to unknown material, possibly contamination (left) and larger dispersoid directly on the carbon tape (right)

4.1.2 Optical Microscopy Phase Analysis

Microstructural evolution was analyzed using image analysis to quantify the phase fraction of Mg_2Si and AlFeSi during homogenization trials. The Si phase could not be identified through optical microscopy and was found with some difficulty in SEM since BSE mode showed little contrast difference between Si and Al. The as-cast Mg_2Si remained in the homogenized billets for all times under 4 hours, and very small amounts were found in the alloy 14 after 4 hrs at 550°C in optical microscopy and confirmed by SEM EDS. In Figure 25 micrographs of undissolved Mg_2Si are shown. The dissolution of Mg_2Si during homogenization of 6082 was modeled by Sarafoglou who found good agreement with experimental results. For an estimated grain diameter of 20-200 μm and an initial Mg_2Si volume fraction of 0.31 - 0.36%, the model estimated full Mg_2Si dissolution in slightly under 3 hours at 560°C but experimental results in this study found

traces of Mg_2Si in the 4-hour homogenization. Mg_2Si dissolution in this system is limited by solute diffusion rather than phase dissolution [23]. The results of this modeling and experimental testing are in good agreement with the observations in this work. The Mg_2Si fraction in these alloys is likely to be higher than what was modeled by Sarafoglou, a consequence of the higher Mg and Si content in the current study alloys. This would suggest a slightly longer time for complete dissolution, possibly approaching the 4-hour mark, which matches the observations for the 2 and 4-hour conditions.

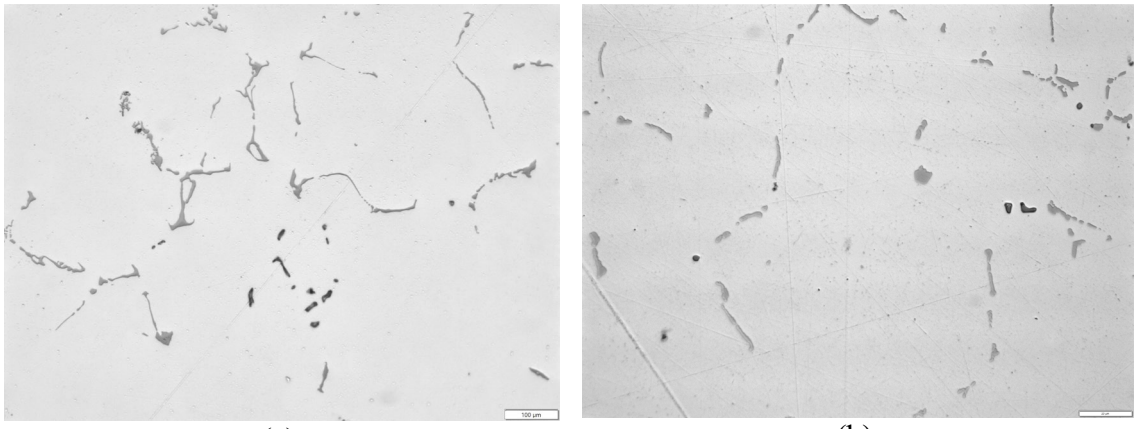

(a) (b)

Figure 25. Undissolved Mg_2Si (black) in (a) 0 hour samples (b) 4 hour sample at 550°C. 500x

According to the XRD phase analysis, no ß → α AlFeSi transformation occurred in either alloy, and the metrics used to evaluate AlFeSi phase morphology are consistent with this observation. During homogenization coarsening or rounding of the primary AlFeSi phase may occur causing some change in morphology and resulting in a dispersoid free zone (DFZ) around the primary particles, which is observed at longer times. This effect may be observed in the increasing shape factor, decreasing perimeter, or decreasing max extent with increasing homogenization time. This was not observed

for changes in homogenization temperature and the changes for homogenization time were small and not statistically significant. The relative consistency in all AlFeSi measurements across the 15 different homogenization conditions does support the absence of ß-AlFeSi consistent with XRD phase identification results

4.2 Dispersoid Structure

The immediate effects of temperature on the appearance of the dispersoids in the matrix were not clear, however time made an obvious and gradual difference. The 0-hour homogenization showed a high dispersoid density which decreased significantly with 2- and 4-hour homogenizations. Large, elongated dispersoids were also found in every sample and were confirmed as dispersoids with EDS. These large particles were around DFZ zones that formed in grain interiors as opposed to the DFZ that form at grain boundaries near primary AlFeSi. These were not, however, found in the 2-step homogenization sample which showed a uniform, homogeneous dispersoid distribution throughout (Figure 26). DFZ's are typically found around primary AlFeSi particles where dissolution of dispersoids leads to coarsening of the primary particles. This was observed in both one and two-step samples. However, the high heating rate of the one-step conditions led to the formation of DFZ at grain centers as well due to the inhomogeneous distribution of *ß'* during high heating rates.

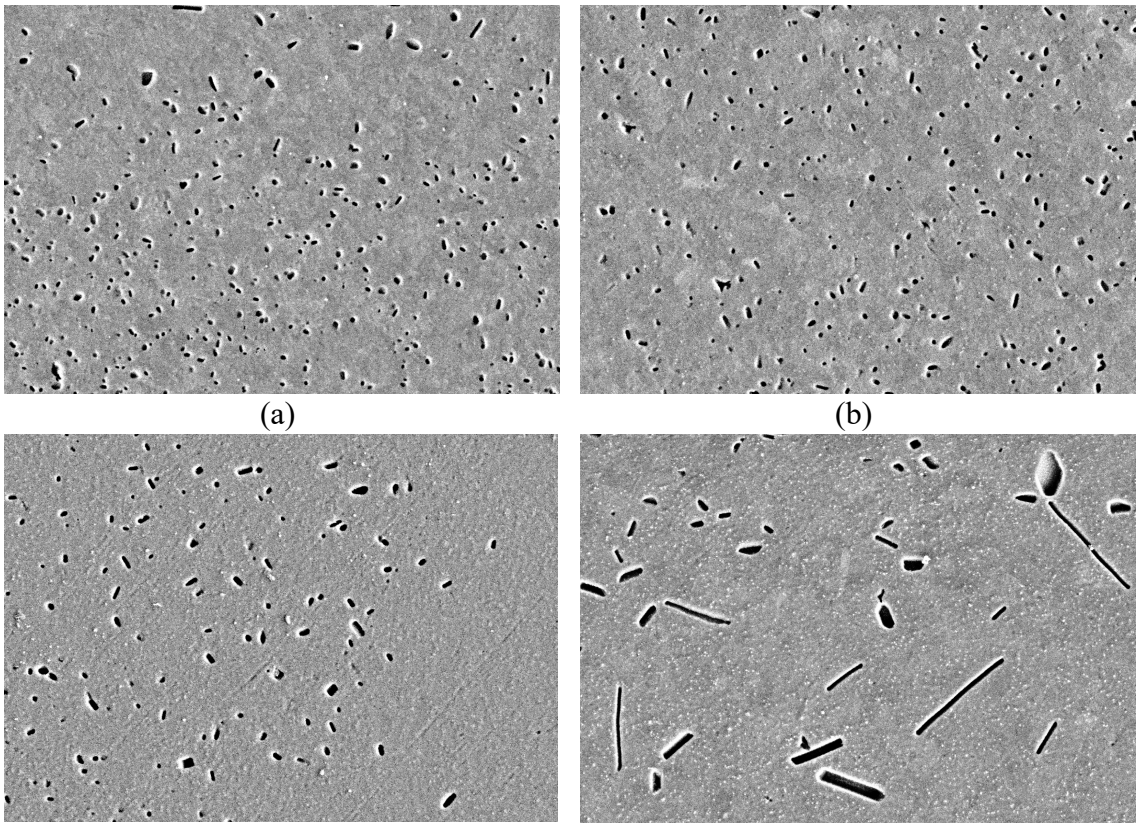

Figure 26. Homogenization at 0 hour (a) 4 hours (b) 12 hour (c) and coarse dispersoids at grain interior in DFZ for 8 hour sample (d)

The effect of temperature on dispersoid density can be observed as a function of homogenization time as originally shown in Figure 17. For every 10°C increase in temperature there was a 5-15% drop in dispersoid number density. This was not consistent in alloy 14, but the trend was present in alloy 16 for all times and temperatures except the 2-step treatment. For temperatures that did show a decrease in dispersoid density it was found to be statistically significant. The increase, or lack of change, in some conditions is most likely caused by limitation in imaging and sampling. Sampling error originating from low dispersoid density in DFZs. Purposefully omitting these areas

and trying to focus on areas with high dispersoid density created issues with biased sampling so a random sampling strategy was maintained.

4.3 Homogenization Ramp Rate Effects

Coarse, elongated dispersoids were found in all samples except the 2-step conditions, regardless of the soak time or temperature. The heating rate of the homogenization treatment is well known to affect the nucleation and later distribution of the precipitates. Nucleation of Mn-containing dispersoids occurs on ß'- Mg_2Si precipitates that form during ramping. Excessive heating rates prevent uniform precipitation of the ß' phase which can lead to non-uniform dispersoid distribution, a larger range of dispersoid sizes, and formation of large DFZs near grain centers. This effect was first documented by Lodgaard and Ryum and later investigated further by Hu and is confirmed in this work. While faster ramp rates were chosen to highlight the differences in soak times and minimize the influence of heating, it did lead to some non-uniform dispersoid formation throughout the microstructure as in Figure 26.

The two-step homogenizations, however, were heated with controlled ramp rates that would be similar to those for commercial billet homogenization. The 2-step homogenization first soaked at 250°C allowing diffusion and precipitation of the ß' phase prior to dispersoid formation. The intent of this was to increase dispersoid uniformity, increase dispersoid nucleation, and reduce final soak time while maintaining dispersoid count. The difference in dispersoid uniformity is obvious as seen in Figure 27. The 2-step dispersoid number density was the second highest, behind the 0-hour homogenization,

despite having a total time above dispersoid nucleation temperatures exceeding that of the 4-hour samples.

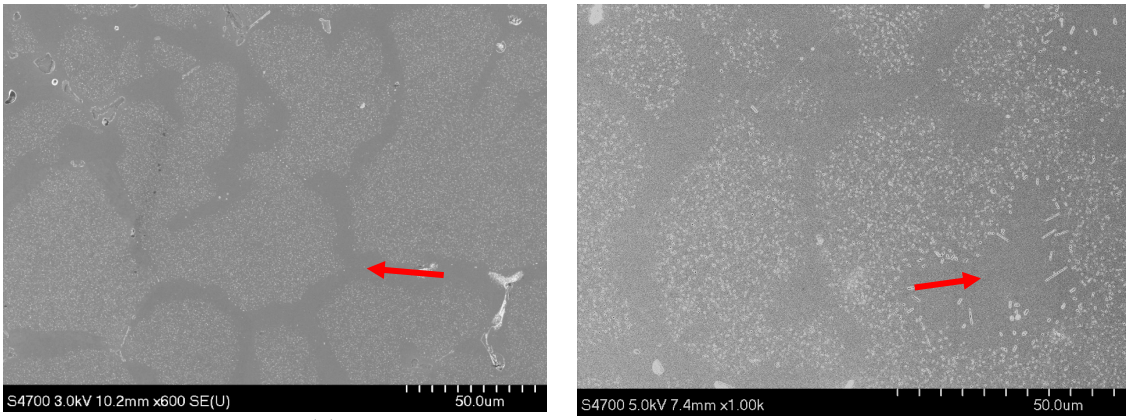

(a) (b)

Figure 27. Uniform dispersoid distribution in alloy 14 2-step at 550°C observed using SEM (a) DFZ and coarse dispersoids in a sample with rapid heating rate in alloy 14, 8 hour, 550°C (b).
Red arrows point to DFZ near primary particles (a) and at grain centers in one-step (b)

4.4 Dispersoid Density

The general trend of decreasing dispersoid density with higher times and temperatures is expected and can be explained by nucleation and growth kinetics. The two-step treatment, which cannot be compared easily to other conditions, also would follow the same mechanisms. The effect of dispersoid size and number density with respect to homogenization time and temperature has been studied in many alloys and homogenization conditions. Mn-containing dispersoids begin nucleation at 400°C while Cr-containing dispersoids begin at 490°C with slower kinetics, resulting in lower overall Cr dispersoid formation [20]. The soak temperatures here far exceed the dispersoid nucleation range shifting the predominant homogenization to growth instead of nucleation. The 0-hour samples had the highest density and smallest dispersoid size by a large margin. With

increasing temperature, dissolution and coarsening of dispersoids occurred resulting in lower number density, larger average size, and a range of sizes (sigma). The difference in heating time between the 3 temperatures for the 0-hour condition was minimal yet the lower dispersoid density for higher temperatures was significant. This same trend was observed for all temperatures where the heating time was insignificant compared to the soak time. This suggests that dispersoid nucleation occurs entirely within the ramping period and any subsequent soaking is coarsening the nucleated phases. This would explain the nearly identical trend in dispersoid density for homogenization at all times in alloy 16. Increasing homogenization temperature increases the diffusion rate of Fe and Cr [20], [23]. Increasing homogenization temperature also will lower the driving force for any dispersoid nucleation that occurs at the soak temperature. Thus, an increase in temperature has a two-fold effect on the dispersoid density: increasing diffusion rate of the slow diffusing Fe and Mn phase in the matrix and lowering the driving force for nucleation of dispersoid phases. A general, but inconsistent, decrease in volume fraction was observed with convergence of volume fraction for all temperatures at the 12-hour condition. This metric is complicated by the etching procedure used, the irregular shape of some larger dispersoids, and variability in sampling due to DFZ's present. The similar area fraction of the 12-hour condition could be explained by higher hold times leading to convergence of dispersoid size as the phase fraction approaches equilibrium and coarsening slows due to decreased surface area of dispersoids.

4.5 Conductivity, Flow Stress, and Dispersoid Correlations

Both conductivity and flow stress followed the trends observed with the dispersoid density and size. These metrics are more difficult to tie directly to homogenization time and temperature and are best explained by the effect changing dispersoid density has on the overall system microstructure. Conductivity in aluminum is lowered by any solid solution alloying elements that exist within the matrix, with precipitation of secondary phases gradually increasing conductivity. The 12-hour samples had the highest conductivity, in which excessive soak times allowed for more coarsening to occur and the Mn and Cr content begins to reach equilibrium values [34]. The increase in conductivity with temperature can be attributed to the increased diffusion rate and the increased solubility of precipitate forming elements, particularly Mn and Cr, as the solubility and contribution of Fe is negligible, as explained by Liu [47]. During shorter homogenization times where smaller dispersoids are dissolving there is constant diffusion of these elements and upon quenching, the solute atoms in transport become trapped in the matrix. Conductivity was also found to increase with lower homogenization temperature for all times since the solubility of elements is decreasing and lowering the total content in solution at any given time [52]. Mg_2Si was still present in the 0- and 2-hour samples but dissolved into the matrix with longer times. The conductivity contribution of Cr and Mn leaving solution is somewhat offset by the increasing Mg and Si in solution at greater times and temperatures. The two-step samples had conductivity similar to that of the 12-hour condition, the highest of all conditions. It is thought that the additional low temperature soak and slower heating rate to the second soak allowed for more time in the

precipitation regime of the *ß'* phase which led to increased precipitation of dispersoids. The increased precipitation of dispersoids decreased the Mn concentration within the matrix, lowering the overall conductivity. Since the soak temperature is primarily coarsening dispersoids, rather than precipitation of Mn dispersoids from the matrix, it would follow that the Mn content would lower with the heating conditions in the two-step samples.

Despite difficulties in the compression testing, use of a maximum flow stress under 0.1 strain was found to have good correlations with homogenization time and especially temperature. Testing was performed in such a way that samples homogenized at the same temperature were tested in close succession. Flow stress alone is complex and difficult to model with dispersoids microstructures, particularly at high temperature where additional deformation mechanisms are active [38]. Interactions between conductivity and flow stress are plotted against dispersoid size, count, sigma, homogenization time, and temperature. The initial assumptions were that increasing dispersoid density would increase conductivity and flow stress, but the relationship to dispersoid size, distribution, and area fraction was unclear. Due to the etching procedure used, the measured area was a function of the size of the etched dispersoids which could overestimate smaller particles and complex shapes. An estimated area fraction was calculated using the mean dispersoid size and the dispersoid count for each homogenization condition and will be labeled calculated area. The difference between the calculated area and the true measured area can be found in the Appendix . Interaction plots of dispersoid size, area fraction, and

dispersoid count were made with conductivity, estimated flow stress, and sigma. Time and temperature interactions for both alloys were clear, as longer times and higher temperatures leads to increased dispersoid size and lower number density. Alloy 14 interactions for time, temperature, conductivity, and flow stress are in Figure 28.

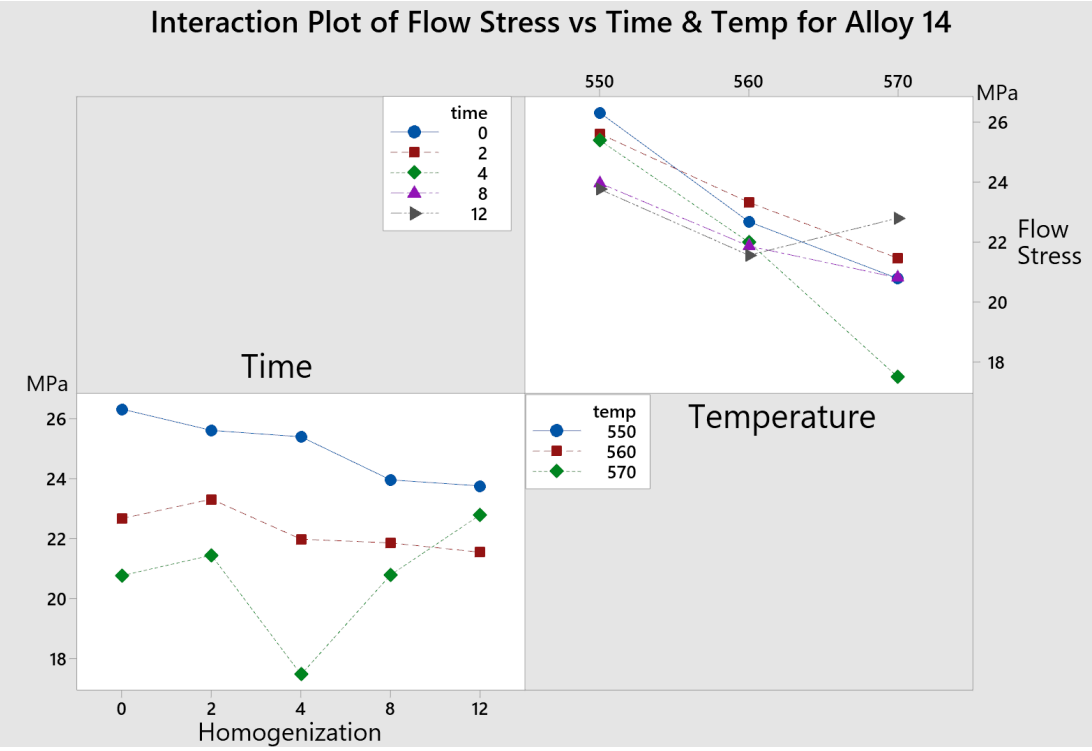

Figure 28. Interaction plot of time, temperature, and flow stress for Alloy 14. Higher temperatures and longer times decrease flow stress

Flow stress and conductivity, which are likely to be a function of dispersoid density, are well correlated to time and temperature but the underlying mechanisms are not clear. Increasing homogenization temperature lowered flow stress, which correlates with the decrease in dispersoid density and increased size as seen previously in Figure 17 and Figure 19, while longer times seems to have the same effect but are less significant. Breaking these effects down further it is possible to generate basic models for estimating

flow stress and conductivity of the material using the time and temperature alone. With a 5 x 3 matrix of time and temperature, a response surface regression can be generated. A model using the factors of time and temperature to predict dispersoid density and size was created. Time was the most significant factor for both models which is expected given the extended range of times used in the homogenization treatments. Temperature was only significant in alloy 16 where the trends in dispersoid size measurements was stronger. For alloy 16 dispersoid count and size the adjusted R^2 value of 91.8% and 89.7%, respectively. In alloy 14 the R^2 values were 82.9% and 91.0% for count and size, respectively. The low significance of temperature in alloy 14 is likely due to sampling error in dispersoid measurements rather than actual differences in dispersoid formation. The graphs for alloy 14 can be found in C

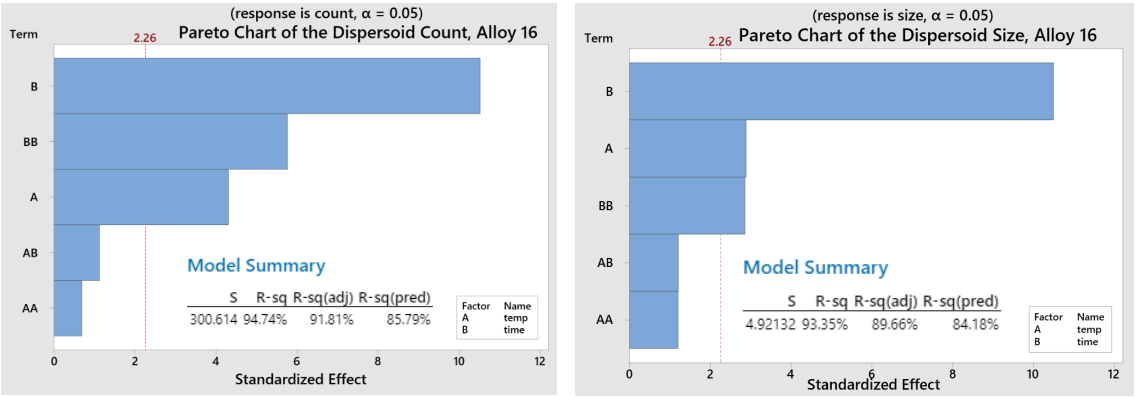

Figure 29. Alloy 16 pareto charts of dispersoid size (a) and count as a function of time and temperature (α = .05). Temperature and time were observed to be significant in both cases. Temperature was more significant in count.

Other responses can be related to dispersoid count and size, and interactions plots of conductivity, flow stress, and calculated area grouped by homogenization temperature

were created to understand the connections dispersoid measurements and other metrics. These interaction plots are shown in Figure 30 and Figure 31

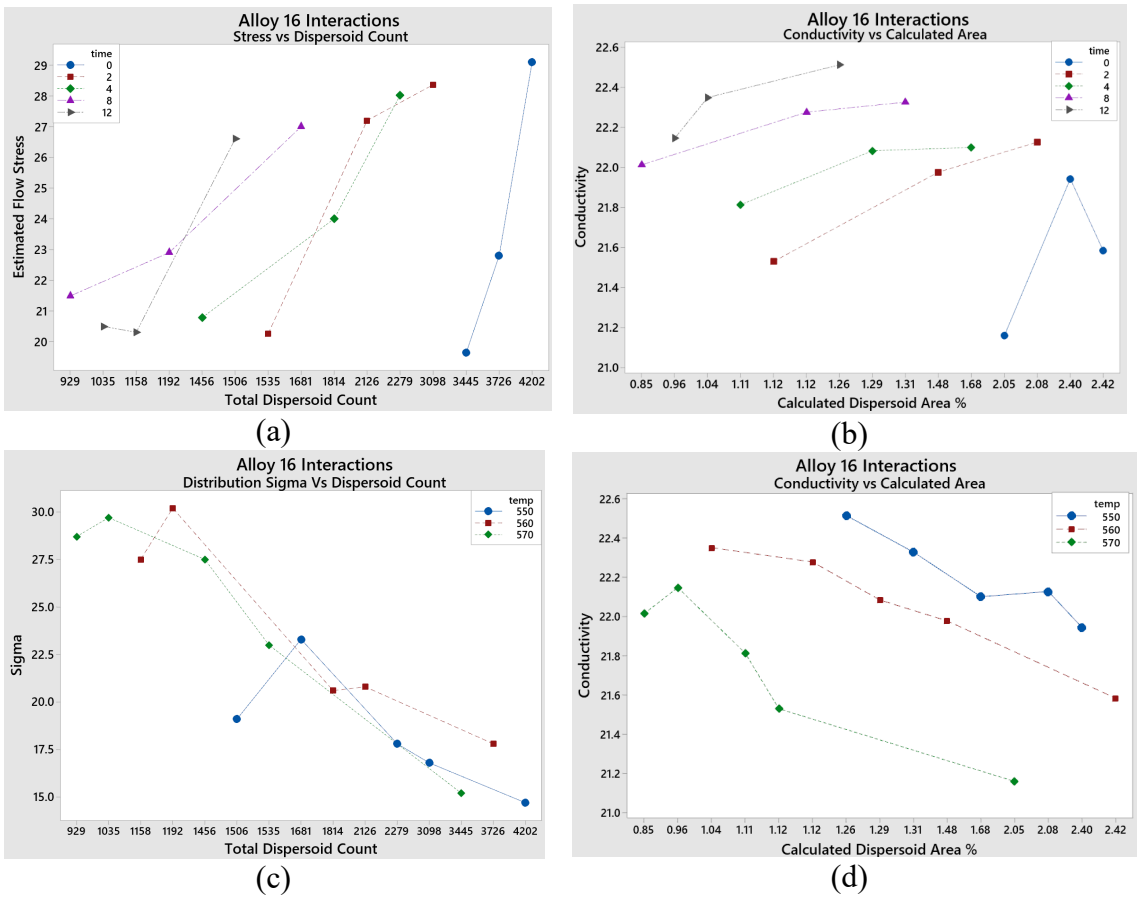

Figure 30. Alloy 16 interactions (a) stress vs count (a) conductivity vs calc area (b) sigma vs count (d) conductivity vs calc area (d), by temperatures.

The correlations for alloy 14 were not as strong as in alloy 16. This was also observed in earlier measurements with dispersoid density and size, and this weaker signal produces noisier trends. Once again, the calculated dispersoid area is well correlated with the total dispersoid count as the area is derived from the count and average size.

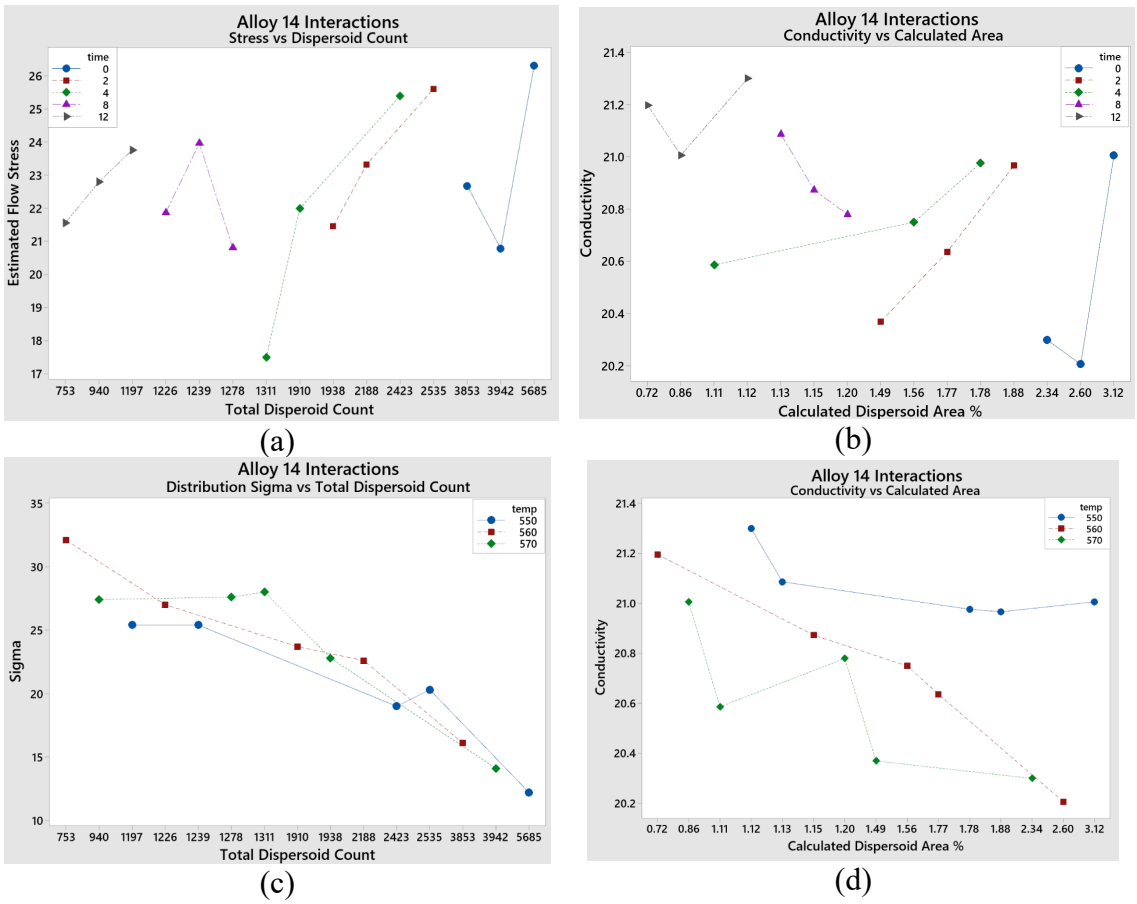

Figure 31. Alloy 14 interactions (a) stress vs count (a) conductivity vs calc area (b) sigma vs count (d) conductivity vs calc area (d), by temperatures.

The estimated flow stress was found to have a strong interaction with the total dispersoid count when grouped by homogenization time in both alloys. Dispersoid size had weaker correlation in alloy 14 but similar correlation to count. The increase in high temperature flow stress with increasing dispersoid density can be explained by assuming Orowan strengthening, where the presence of intermetallic phases within the matrix serves as obstacles to dislocations increasing the stress for during deformation. This effect is diminished at higher temperatures where dislocation climb is more prevalent however some strengthening remains even at higher temperatures [38]. The effect of

solid solution strengthening in aluminum is well studied, but the combined contribution by dispersoids and solid solution strengthening by Mn, Si, and Mg in solid solution is difficult to properly analyze and model [67], [68]. In this analysis the basic assumptions of increased strength with higher dispersoid density and higher solute concentration explain the trends quite well. It is unclear the degree to which the solid solution strengthening of Mn vs Mg has on the flow stress. In solid solution, the Mn content is expected to decrease with time and temperature while Mg and Si are thought to increase, at least for the 0 – 4 hr homogenization conditions. The inverse relationship of these elements in solution complicates understanding the flow stress. For the longer homogenization times where Mg_2Si was fully dissolved, the contribution to flow stress would remain constant yet the dispersoid density and flow stress continue to decrease with increasing temperature. The dispersoid contribution to flow stress through Orowan strengthening would be more significant than the effect of Mg, Si, and Mn solid solution strengthening, at least within the accuracy of the tests that were performed here. Increasing time significantly decreased the dispersoid count and increased size, but only lead to a minor decrease in the flow stress over the 5 homogenization times suggesting the total strengthening by dispersoids is small. Work to explain these multiple effects in a comprehensive model of flow stress is an active area of research but a challenging task. Deformation mechanisms based on solute concentration, primary intermetallic size and volume fraction, additional testing temperatures, and strain rate sensitivity all must be considered for a more accurate model depicting the flow stress of this material [8], [47], [69]. Nonetheless, a clear trend of decreasing flow stress with increasing homogenization

temperature and total dispersoid count was observed in both alloys at temperature increments of 10°C.

Conductivity in aluminum is known to be heavily dependent on the alloying elements present in solid solution, volume fraction of secondary phases, grain boundaries, solute clusters, and other microstructural components. Elements in solid solution play a significant role in precipitation alloys like 6082, so elements as Mn, Mg, Si, Fe, and Cr, will change the conductivity of the alloy during heat treatments and precipitation of secondary phases. Based on dispersoid density and size observed here, it was thought that nucleation occurs quite quickly during heating, drawing Mn, Fe, and Si out of solution to form dispersoids, and then following this coarsening occurs, decreasing the particle count. As homogenization temperature increases the diffusion rate and solubility, the rate of dispersoid growth increases as well. At the end of the homogenization cycle when the samples are quenched any alloying elements remaining in solution will become trapped forming a supersaturated solid solution. The increased conductivity with longer homogenization times can be attributed to the solid solution content and dispersoid phase fraction approaching equilibrium values as coarsening slows. The constant dissolution of small dispersoids during this time frame will decrease the resulting conductivity. One unavoidable consequence of the short homogenization times is the presence of Mg_2Si in samples with 0- and 2-hour cycles. This would decrease the conductivity as dissolution occurs but the increase associated with the precipitation of dispersoids, has a greater significance than Mg and Si in solution for the alloying content being studied here [70].

No interaction between sigma and the measure conductivity or flow stress could be found that was not adequately described by the dispersoid size and number density already. Sigma was well correlated with the measured dispersoid size and density. The width of the dispersoid size distribution, denoted as sigma in the logistic model used to fit them, decreased with higher dispersoid densities i.e., lower times and temperatures. There was also noticeable increase in sigma with increases in temperature in the interaction plots. It follows that with increased temperature, diffusion kinetics, and growth, the coarsening of the particles will lead to a greater distribution of sizes as small particles dissolve and decrease in number while large particles remain. This trend fits well with the mechanisms used to describe the conductivity, dispersoid size, and number density previously.

4.6 2-step Homogenization Significance

The 2-step homogenization conditions were not used when creating the interaction plots or models. The slow heating rate and additional soak of the 2-step cycle resulted in outliers when comparing all conditions based on soak time, soak temperature, or dispersoid number density. The same trend relating the decreased dispersoid density with increased temperature remained, however. It can be concluded, then, that the small increase in homogenization temperature is not dependent on the heating rate of either the single step or 2-step homogenizations. The mechanisms are likely entirely growth controlled where higher temperatures will increase diffusion and growth kinetics of dispersoids. The overall dispersoid count and size was comparable to that of the 2-hour

homogenization despite holding for twice the time. The slower ramp rates resulted in a more uniform dispersoid distribution, which may create an artificially higher dispersoid density when compared to a sample which had large DFZ or exceedingly large, needle-like dispersoids formed by the higher heating rate. However, if areas only containing high dispersoid density with uniform distribution are counted in both samples it is still found that number density is higher in the 2-step homogenization. The average dispersoid size in the two-step samples was greater than that of equivalent temperatures in 2 hour one-step samples which is expected for the longer soak time of 3 hours. The higher dispersoid density and simultaneously increased dispersoid size supports the claim that slower ramping and additional low temperature soaking can increase dispersoid density and high temperature soak only results in coarsening of dispersoids. In industrial one-step homogenization, the time spent in the dispersoid nucleation and growth temperature regime is much higher due to the much slower heating of large billets before soaking is started. Consequently, the dispersoid density measured in the 0, 2, and 4 hour samples here should be higher than samples using slower, more realistic ramp rates. Yet, the 2-step homogenization, which used heating rates from industry, defied this and showed the second highest dispersoid density of all samples. Recent work by Remøe found that high heating rates, slightly slower than what was used here, resulted in a higher dispersoid density for 6082 alloys suggesting that nearly complete precipitation of dispersoids does occur. The dispersoid nucleation on ß' precipitates and significance of heating rates in ß' precipitation regime, originally presented by Lodgaard and Ryum and later investigated by Schiffl for 2-step homogenization, support the findings here [20], [27].

4.7 Conclusions and Applicable Results

The results of this experiment have provided guidance on optimizing the homogenization process, specifically in high strength 6082 alloys. An etching method was developed and compared against standard BSE imaging of dispersoids and was found to give similar but not identical results on the dispersoid count and size. This technique can serve as an alternative to BSE dispersoid imaging or help distinguish dispersoids from other high content phases that may appear in BSE imaging. Maximizing dispersoid density and reducing size is possible with lower temperatures and times as variations of 10-20°C can significantly reduce the dispersoid content and properties. The minimum homogenization time for this alloy specifically can be set by the dissolution of Mg_2Si and element Si phases as no as-cast ß → α AlFeSi transformation was observed, and minimal morphological changes occurred in the α phase even at 12-hour homogenization times. Application of intermetallic particle extraction using the phenol dissolution technique was successful, and new observations on this techniques were reported. For modifying billet homogenization procedures, the minimum soak time and ramping rate are dependent on billet dimensions and other physical constraints. Excessively fast heating will result non-uniform dispersoid distribution, but such heating rates are unrealistic beyond laboratory testing, yet the effect of soak temperature variations on dispersoid density remains and appears to occur regardless of the heating rate. Experiments using 2-step homogenization processes to promote higher dispersoid density with shorter soak times were tested. These yielded novel experimental results on

the effects of a two-step process with varied homogenization temperature and the effects it has on the unique two-step homogenization process.

5 Reference List

[1] "Aluminum: Competitive Conditions Affecting the U.S. Industry," p. 610.

[2] "Uses of Aluminum Extrusions | Hydro Extrusion North America." https://www.hydro.com/en-US/aluminum/products/extruded-profiles/north-america-resources/extruded-aluminum-products/uses-of-aluminum-extrusions/ (accessed Jun. 17, 2021).

[3] "What are Aluminum Extrusions used for? | AEC." https://www.aec.org/page/extrusion-applications (accessed Jun. 17, 2021).

[4] O. Reiso, *Extrusion of AlMgSi Alloys*.

[5] "Do you know when to use the indirect extrusion process?" https://www.shapesbyhydro.com/en/expert-thoughts/do-you-know-when-to-use-the-indirect-extrusion-process/ (accessed Aug. 12, 2021).

[6] "aluminium-in-cars-unlocking-the-lightweighting-potential.pdf." Accessed: Jun. 29, 2021. [Online]. Available: https://www.european-aluminium.eu/media/1326/aluminium-in-cars-unlocking-the-lightweighting-potential.pdf

[7] marshall, "Fabricated Aluminum Bikes are Stronger, Faster, Lighter," *Taber Extrusions*, Mar. 07, 2018. https://taberextrusions.com/fabricated-aluminum-bikes-stronger/ (accessed Jun. 29, 2021).

[8] X. Qian, N. Parson, and X.-G. Chen, "Effects of Mn content on recrystallization resistance of AA6082 aluminum alloys during post-deformation annealing," *Journal of Materials Science & Technology*, vol. 52, pp. 189–197, Sep. 2020, doi: 10.1016/j.jmst.2020.04.015.

[9] "Heat Treating of Aluminum Alloys," p. 39.

[10] G. Valder, "Billet homogenizing – Batch or continuous?" Otto Junker.

[11] B. Treanore, "MTU statement of work.pdf." Michigan Technological University.

[12] U. Tundal and O. Reiso, "Method for Producing a Heat Treatable Aluminium Alloy with Improved Mechanical Properties," 20180282849, Oct. 04, 2018 Accessed: Feb. 06, 2021. [Online]. Available: https://www.freepatentsonline.com/y2018/0282849.html

[13] S. K. Das, "Modeling and Optimization of Direct Chill Casting to Reduce Ingot Cracking," p. 74.

[14] D. Eskin, “Mechanisms of Macro-Segregation in Direct-Chill Casting of Aluminum Alloys,” p. 8.

[15] T. Sheppard, *Extrusion of Aluminium Alloys*. Boston, MA: Springer US, 1999. doi: 10.1007/978-1-4757-3001-2.

[16] S. Kumar, P. S. Grant, and K. A. Q. O’Reilly, “Evolution of Fe Bearing Intermetallics During DC Casting and Homogenization of an Al-Mg-Si Al Alloy,” *Metall Mater Trans A*, vol. 47, no. 6, pp. 3000–3014, Jun. 2016, doi: 10.1007/s11661-016-3451-5.

[17] H. Tanihata, T. Sugawara, K. Matsuda, and S. Ikeno, “Effect of casting and homogenizing treatment conditions on the formation of Al–Fe–Si intermetallic compounds in 6063 Al–Mg–Si alloys,” *Journal of Materials Science*, vol. 34, no. 6, pp. 1205–1210, Mar. 1999, doi: 10.1023/A:1004504805781.

[18] A. Woźnicki, D. Leśniak, G. Wloch, B. Leszczyńska-Madej, and A. Wojtyna, “The Effect Of Homogenization Conditions On The Structure And Properties Of 6082 Alloy Billets,” *Archives of Metallurgy and Materials*, vol. 60, pp. 1763–1771, Oct. 2015, doi: 10.1515/amm-2015-0303.

[19] M. Cieslar, J. Bajer, M. Hájek, and V. Očenášek, “High-Temperature Processes Occurring during Homogenization of AA6082 Aluminum Alloy,” in *Light Metals 2014*, J. Grandfield, Ed. Hoboken, NJ, USA: John Wiley & Sons, Inc., 2014, pp. 237–241. doi: 10.1002/9781118888438.ch41.

[20] L. Lodgaard and N. Ryum, “Precipitation of dispersoids containing Mn and/or Cr in Al–Mg–Si alloys,” *Materials Science and Engineering: A*, vol. 283, no. 1, pp. 144–152, May 2000, doi: 10.1016/S0921-5093(00)00734-6.

[21] R. Hu, T. Ogura, H. Tezuka, T. Sato, and Q. Liu, “Dispersoid Formation and Recrystallization Behavior in an Al-Mg-Si-Mn Alloy,” *Journal of Materials Science & Technology*, vol. 26, no. 3, pp. 237–243, Mar. 2010, doi: 10.1016/S1005-0302(10)60040-0.

[22] D. Lassance, M. Schmitz, F. Delannay, and T. Pardoen, “Linking microstructure and high temperature ductility in aluminium alloys 6XXX,” *11th International Conference on Fracture 2005, ICF11*, vol. 6, pp. 4099–4104, Jan. 2005.

[23] P. Sarafoglou and G. Haidemenopoulos, “Phase Fraction Mapping in the as-cast microstructure of extrudable 6xxx aluminum alloys,” *International Journal of Materials Research (formerly Zeitschrift fuer Metallkunde)*, vol. 105, Dec. 2014, doi: 10.3139/146.111139.

[24] R. Dickson, “Thermomechanical Processing and Temperature measurement,” presented at the June 2020 Webinar, Hydro Aluminum Technology Center.

[25] J. Asensio-Lozano and B. Suarez-Peña, “Effect of the addition of refiners and/or modifiers on the microstructure of die cast Al–12Si alloys,” *Scripta Materialia*, vol. 54, no. 5, pp. 943–947, Mar. 2006, doi: 10.1016/j.scriptamat.2005.10.067.

[26] R. Aagård, “Effect of Mn and Dispersoids on Grain Structure, Mechanical Properties and Crush Behavior of Extruded AA6082 Alloys,” p. 102.

[27] A. Schiffl, A. Arnoldt, D. Hillebrand, and J. Österreicher, “The Influence of different homogenization regimes on the recrystallization stability of 6082 with different Mn and Cr contents,” p. 7.

[28] N. W Kuijpers, F. Vermolen, K. Vuik, and S. Zwaag, “A Model of the β-AlFeSi to α-Al(FeMn)Si Transformation in Al-Mg-Si Alloys,” *Materials Transactions*, vol. 44, no. 7, pp. 1448–1456, 2003, doi: 10.2320/matertrans.44.1448.

[29] M. Bru, “The Effect of Mn and Homogenisation Procedure on Mechanical Properties and Grain Structure in Extruded AA6082,” p. 83.

[30] “Effects of Extrusion Parameters on Coarse Grain Surface Layer in 6xxx Series Extrusions,” p. 12.

[31] Y. Birol, “Impact of partial recrystallization on the performance of 6005A tube extrusions,” *Engineering Failure Analysis*, vol. 17, no. 5, pp. 1110–1116, Jul. 2010, doi: 10.1016/j.engfailanal.2010.01.006.

[32] J. A. Blind and J. W. Martin, “The Effect of Dispersoids on the Ductile Fracture Toughness of AI-Mg-Si Alloys,” p. 6.

[33] B. Milkereit and M. J. Starink, “Quench sensitivity of Al–Mg–Si alloys: A model for linear cooling and strengthening,” *Materials & Design*, vol. 76, pp. 117–129, Jul. 2015, doi: 10.1016/j.matdes.2015.03.055.

[34] A. D. Kubiak, “EFFECT OF HOMOGENIZATION ON HIGH TEMPERATURE DEFORMATION BEHAVIOUR OF AA3XXX ALUMINUM ALLOYS,” p. 128.

[35] S. Pogatscher, H. Antrekowitsch, H. Leitner, D. Pöschmann, Z. L. Zhang, and P. J. Uggowitzer, “Influence of interrupted quenching on artificial aging of Al–Mg–Si alloys,” *Acta Materialia*, vol. 60, no. 11, pp. 4496–4505, Jun. 2012, doi: 10.1016/j.actamat.2012.04.026.

[36] A. Bahrami, “Modeling of precipitation sequence and ageing kinetics in Al-Mg-Si alloys.,” [s.n.], S.l., 2010.

[37] G. Mrówka-Nowotnik, J. Sieniawski, and M. Wierzbiñska, “Intermetallic phase particles in 6082 aluminium alloy,” *Archives of Materials Science and Engineering*, vol. 28, no. 2, p. 8.

[38] C. Liu, “MICROSTRUCTURE EVOLUTION DURING HOMOGENIZATION AND ITS EFFECT ON THE HIGH TEMPERATURE DEFORMATION BEHAVIOUR IN AA6082 BASED ALLOYS,” p. 226.

[39] A. Rollett, F. J. Humphreys, G. S. Rohrer, and M. Hatherly, *Recrystallization and Related Annealing Phenomena*. Elsevier, 2004.

[40] A. Eivani, S. Valipour, H. Ahmed, J. Zhou, and J. Duszczyk, “Effect of size distribution of nanoscale dispersed particles on the Zener drag pressure,” *Metallurgical and Materials Transactions A*, vol. 42, no. 4, pp. 1109–1116, 2011.

[41] J. V. Jakobsen, “Microstructure and Mechanical Properties of Welded AA6082 Aluminium Alloys,” p. 106.

[42] Z. Liang, “Clustering and Precipitation in Al-Mg-Si Alloys,” p. 12372 kb, 125 pages, 2012, doi: 10.5442/D0032.

[43] K. Huang, Y. J. Li, and K. Marthinsen, “Effect of heterogeneously distributed pre-existing dispersoids on the recrystallization behavior of a cold-rolled Al–Mn–Fe–Si alloy,” *Materials Characterization*, vol. 102, pp. 92–97, Apr. 2015, doi: 10.1016/j.matchar.2015.02.015.

[44] J. Österreicher, M. Kumar, A. Schiffl, S. Schwarz, D. Hillebrand, and G. Bourret, “Sample preparation methods for scanning electron microscopy of homogenized Al-Mg-Si billets: A comparative study,” *Materials Characterization*, vol. 122, Oct. 2016, doi: 10.1016/j.matchar.2016.10.020.

[45] M. Remøe, I. Westermann, and K. Marthinsen, “Characterization of the Density and Spatial Distribution of Dispersoids in Al-Mg-Si Alloys,” *Metals*, vol. 9, no. 1, p. 26, Dec. 2018, doi: 10.3390/met9010026.

[46] Q. Zhao, B. Holmedal, and Y. Li, “Influence of dispersoids on microstructure evolution and work hardening of aluminium alloys during tension and cold rolling,” *Philosophical Magazine*, vol. 93, no. 22, pp. 2995–3011, Aug. 2013, doi: 10.1080/14786435.2013.794315.

[47] C. Li, K. Liu, and N. Parson, “THE EFFECT OF HEAT TREATMENTS ON PRECIPITATION BEHAVIOR OF DISPERSOIDS IN Al-Mg-Si-Mn ALLOY,” p. 9.

[48] L. Zhang, J. Gao, L. N. W. Damoah, and D. G. Robertson, “Removal of Iron From Aluminum: A Review,” *Mineral Processing and Extractive Metallurgy Review*, vol. 33, no. 2, pp. 99–157, Mar. 2012, doi: 10.1080/08827508.2010.542211.

[49] J. E. Yoo, A. Shan, I. G. Moon, and S. J. Maeng, “A study on composition and crystal structure of dispersoids in AlMgSi alloys,” p. 5.

[50] T. Furu, “(PDF) A Novel Methodology for Optimization of Properties, Costs and Sustainability of Aluminium Extrusions,” *ResearchGate*. https://www.researchgate.net/publication/309620882_A_Novel_Methodology_for_Optimization_of_Properties_Costs_and_Sustainability_of_Aluminium_Extrusions (accessed Sep. 23, 2020).

[51] K. Strobel, M. A. Easton, L. Sweet, M. J. Couper, and J.-F. Nie, “Relating Quench Sensitivity to Microstructure in 6000 Series Aluminium Alloys,” *Mater. Trans.*, vol. 52, no. 5, pp. 914–919, 2011, doi: 10.2320/matertrans.L-MZ201111.

[52] L. Lodgaard, “Precipitation of dispersoids containing Mn and/or Cr in Al-Mg-Si alloys,” NTNU, Trondheim, 2000.

[53] G. Svenningsen, M. H. Larsen, J. H. Nordlien, and K. Nisancioglu, “Effect of high temperature heat treatment on intergranular corrosion of AlMgSi(Cu) model alloy,” *Corrosion Science*, vol. 48, no. 1, pp. 258–272, Jan. 2006, doi: 10.1016/j.corsci.2004.12.003.

[54] M. Stoknes, “Effect of Copper and Zinc on Corrosion Behaviour and Mechanical Properties in 6082-Alloys,” p. 112.

[55] Jon Michalek, M. Capek, and J. Janacek, *Stack Contrast Adjustment Plugin*. [Online]. Available: https://imagej.nih.gov/ij/plugins/stack-contrast/index.htm

[56] I. Arganda-Carreras *et al.*, “Trainable Weka Segmentation: a machine learning tool for microscopy pixel classification,” *Bioinformatics*, vol. 33, no. 15, pp. 2424–2426, Aug. 2017, doi: 10.1093/bioinformatics/btx180.

[57] K. SATO and I. IZUMI, “CHEMICAL ISOLATION OF INTERMETALLIC COMPOUNDS FROM ALUMINIUM AND ITS ALLOYS.” NIKKEI Techno-Research Company, 1984.

[58] S. P. Gupta, “Kinetics of discontinuous coarsening of cellular precipitate in a Cu-15wt%In alloy”.

[59] D. Panahi, “Precipitation of Intermetallic Phases from Rapidly Solidifying Aluminum Alloys,” *Materials Science and Engineering*, p. 153, 2009.

[60] J. de P. Martins, A. L. M. de Carvalho, P. H. F. Oliveira, and A. F. Padilha, “PRECIPITATE EXTRACTION FROM 3003 ALUMINUM ALLOY PRODUCED BY TWIN ROLL CASTING/ EXTRAÇÃO PRECIPITADA DE 3003 LIGAS DE ALUMÍNIO PRODUZIDAS POR FUNDIÇÃO EM ROLO DUPLO,” *BJD*, vol. 7, no. 2, pp. 12057–12069, 2021, doi: 10.34117/bjdv7n2-027.

[61] I. Solli, “Characterization of Iron Bearing Particles in Relation to Fir-Tree Structure in Al-Mg Alloys,” p. 119.

[62] A. L. Dons, “‘Universal’ Laws for the Density of Disperoids after the Homogenisation Heat Treatment of Aluminium,” p. 6.

[63] A. HERNÁNDEZ-RODRÍGUEZ, “EFFECTS OF THE Fe/Mn WEIGHT RATIO AND COOLING RATE ON THE AREA FRACTIONS OF α-AlFeSi AND β-AlFeSi PHASES IN Al-7.5Si-3.75Cu-0.5Mg-0.55Fe-xMn ALUMINUM ALLOY”.

[64] X. Cao and J. Campbell, “Morphology of β-Al5FeSi phase in Al-Si cast alloys,” *Materials Transactions - MATER TRANS*, vol. 47, pp. 1303–1312, May 2006, doi: 10.2320/matertrans.47.1303.

[65] P. I. Sarafoglou, “Development of design rules for high extrudability,” p. 164.

[66] P. Donnadieu, G. Lapasset, and T. H. S. Jr, “ALPHA-PHASE PARTICLES IN 6XXX ALUMINUM ALLOYS,” *THE 4TH INTERNATIONAL CONFERENCE ON ALUMINUM ALLOYS*, p. 8.

[67] Q. Zhao and B. Holmedal, “Effect of Si Additions on Solid Solution Hardening of Al-Mn Alloys,” in *ICAA13: 13th International Conference on Aluminum Alloys*, H. Weiland, A. D. Rollett, and W. A. Cassada, Eds. Hoboken, NJ, USA: John Wiley & Sons, Inc., 2012, pp. 1825–1829. doi: 10.1002/9781118495292.ch273.

[68] Ø. Ryen, B. Holmedal, O. Nijs, E. Nes, E. Sjölander, and H.-E. Ekström, “Strengthening mechanisms in solid solution aluminum alloys,” *Metall and Mat Trans A*, vol. 37, no. 6, pp. 1999–2006, Jun. 2006, doi: 10.1007/s11661-006-0142-7.

[69] W. Ren, C. Xu, and X. Chen, “Hot Deformation Behavior and Dynamic Recrystallization Model of 6082 Aluminum Alloy in High Temperature,” *IOP Conf. Ser.: Mater. Sci. Eng.*, vol. 381, p. 012175, Aug. 2018, doi: 10.1088/1757-899X/381/1/012175.

[70] J. E. Hatch, *Aluminum: Properties and Physical Metallurgy*. ASM International, 1984.

A Hot Compression Results

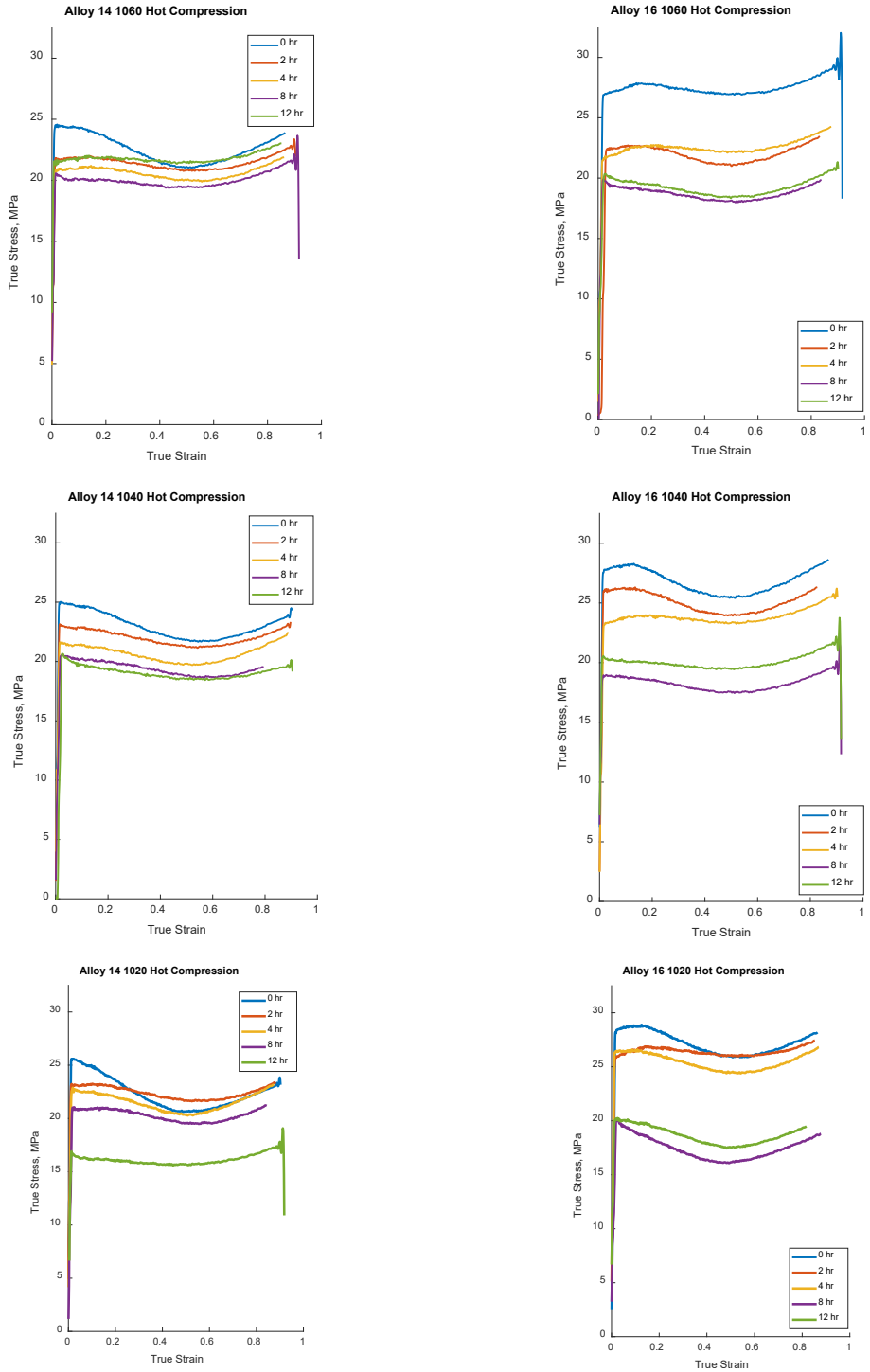

Figure 32. Flow Stress Comparisons for both alloys

B Measured Area vs Calculated Area of Dispersoids

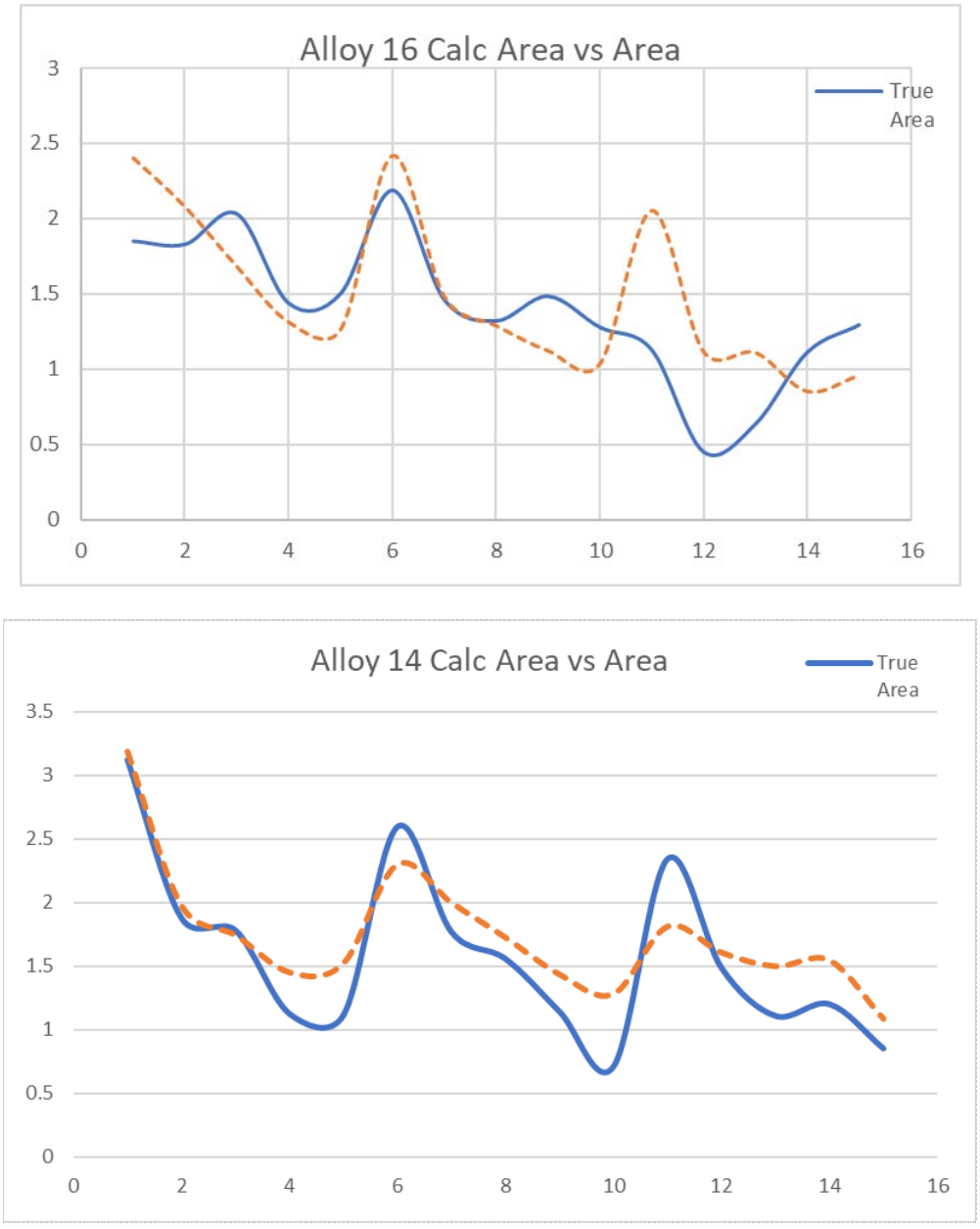

Figure 33. Measured Area vs Calculated

C Alloy 14 Pareto Plots

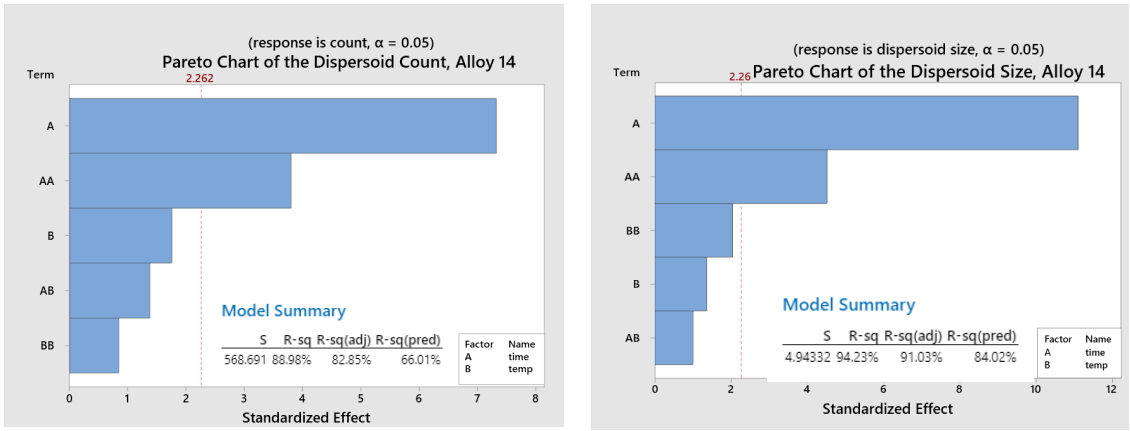

(a) (b)

Figure 34. Alloy 14 pareto charts of dispersoid size (a) and count as a function of time and temperature (α = .05).